
Attosecond Pulse Generation with Annular-Mode Few-Cycle Fields

Johannes Bürger



Munich 2018

Attosecond Pulse Generation with Annular-Mode Few-Cycle Fields

Johannes Bürger

Bachelor's Thesis
at the Faculty of Physics
at Ludwig-Maximilians-University
Munich

submitted by
Johannes Bürger
from Bremen

June 14th, 2018

Examiner: Dr. Martin Schultze

Date of the Oral Examination: June 18th, 2018

Erzeugung von Attosekundenlichtpulsen mit ringförmigen Lasermoden

Johannes Bürger

Bachelorarbeit
an der Fakultät für Physik
der Ludwig-Maximilians-Universität
München

vorgelegt von
Johannes Bürger
aus Bremen

München, den 14. Juni 2018

Gutachter: Dr. Martin Schultze

Tag der mündlichen Prüfung: 18. Juni 2018

Contents

Abstract	ix
1 Introduction	1
2 High harmonic generation (HHG)	5
2.1 Theory of high harmonic generation	5
2.1.1 The three-step model	6
2.1.2 Optimizing the harmonic yield	14
2.2 Experimental implementation of HHG	21
2.2.1 Laser setup	21
2.2.2 Pressure dependence of HHG	24
2.2.3 Carrier-envelope phase (CEP) dependence of HHG	25
3 Beam splitting via holey mirrors	29
3.1 Theory of diffraction for monochromatic light	30
3.2 Theory of diffraction for polychromatic light pulses	32
3.3 Diffraction induced by holey mirrors	34
3.3.1 Influence on the propagation	34
3.3.2 Influence on the focusing properties	37
3.3.3 Effects due to spatio-temporal coupling	44
3.4 Holey mirror beamsplitters in HHG	45
4 Conclusion	47
Bibliography	53
Acknowledgement	54

Abstract

High harmonic generation (HHG) is a key tool for the production of coherent attosecond laser pulses providing experimental access to the ultrafast motion of electrons. In the course of this thesis, we implemented a setup for HHG from gases serving as the front end of a future beamline for attosecond experiments. It is driven by high-intensity femtosecond laser pulses delivered by a carrier-envelope phase (CEP) stabilized source.

We characterized the generated radiation spatially and spectrally by means of an extreme ultraviolet (XUV) CCD camera optionally combined with a grating. Having optimized the mode structure and the intensity of the harmonic beam, we studied the dependence of its spectrum on the target gas pressure and the CEP of the driving field. A shift to higher energies for reduced gas pressures and for the CEP attributed to a cosine waveform were observed. These results are in good agreement with the presented theory.

The second part of the thesis explores the possibility of using holey mirrors as beamsplitters for interferometry applications with broadband pulses. Compared to conventional beamsplitters, they provide the main advantage of not adding any material dispersion to the beams and thereby generate a spectrally and temporally identical pair of pulses. In particular, the diffraction effects introduced by the hole on the focusing properties of two emerging beams are studied. To this end, we calculated the Fresnel diffraction integral numerically for a beam that initially features a Gaussian profile.

The simulation reveals that the reflected annular beam is focused to nearly the same focal shape as the full beam which means that its ability to generate high harmonics is not impaired. A similar focal volume can be achieved for the transmitted round beam albeit with higher distortions occurring at the outer, low-intensity parts of the focus. Due to the smaller beam size, a reduction of the focal length becomes necessary to achieve the desired peak intensity. In order to determine the correct length, we demonstrated that the scaling law of the focal intensity with the focal length is nearly identical to that of a Gaussian beam. In conclusion, it can be stated that holey mirrors are a well-functioning alternative to split a beam of ultrashort laser pulses.

Chapter 1

Introduction

Lasers have been one of the main driving forces of the scientific and technological progress since their invention nearly 60 years ago. Today they serve a wide area of applications like chip manufacturing via photolithography, any form of modern communication via optical fibers, numerous medical therapies, high resolution biological imaging via fluorescence microscopy, gravitational wave detection and the research on quantum computers, just to name a few.

Shortly after the construction of the first laser, a trend started with the goal to increase the peak power of the generated radiation to ever higher levels. This led to the discovery of a wide range of effects that are only observable at high light intensities and opened the sprawling field of nonlinear optics. For example, it is possible to combine two photons into one that carries the sum or difference of their energies, a high intensity laser beam will be focused spontaneously when propagating through any material including air and atoms can be ionized with multiple photons all carrying energies of less than the ionization potential.

These discoveries are mainly based on the improvement of pulsed lasers which can compress a given pulse energy to a very short time interval and thus reach unprecedented peak powers up to the petawatt regime [1] - that is approximately the total power of one million power plants. This development has its origin mainly in the availability of reflective optics and laser media which support the broad frequency range needed to generate ultrashort pulses. For the experiments in this thesis for example, laser pulses with femtosecond duration (10^{-15} s) are used whose spectra extend from the blue part of the visible up to the near infrared. Taking into account that one of these pulses is only generated about every millisecond - i.e. 10^{12} times longer than its duration - the strong concentration of energy becomes apparent.

Although femtosecond laser pulses are already sufficiently short to study the motion of atoms, they cannot resolve the dynamics of their electrons which move on the timescale of attoseconds (10^{-18} s) due to their about three orders of magnitude lower mass. Yet,

the presently supported wavelength range of optical resonators does not allow to directly generate pulses with durations below the femtosecond regime. This is founded on the fact that a pulse cannot be made much shorter than one oscillation of its carrier frequency - a limit that is already reached by current setups. Further reducing the central wavelength to the ultraviolet spectral range is not feasible because this radiation is absorbed strongly by most materials and the losses introduced by currently available mirror coatings would prevent the buildup of radiation in a laser cavity.

In order to achieve even shorter pulse durations, a viable alternative was discovered in the 1980s: When focusing high intensity laser pulses onto a gas target, the generation of high multiples of the laser frequency reaching up to several hundred orders could be observed [2, 3]. Remarkably, the spectrum of this radiation did not show the strong decline with increasing energy which was known for other nonlinear processes. On the contrary, it exhibited a plateau-like structure followed by a sharp cutoff. This phenomenon is known today as high harmonic generation (HHG) and can be explained by the so called three-step model developed by Corkum in 1993 (cf. Sec. 2.1.1). The temporal profile of the generated radiation is typically a train of pulses with attosecond durations and central wavelengths reaching down to the extreme ultraviolet (XUV) or soft X-ray spectral range. In 2001 Hentschel et al. demonstrated the isolation of a single attosecond pulse for the first time which can be regarded as the starting point of attosecond physics [4].

In the course of this thesis, HHG from gases is examined including the implementation of a setup that will serve as a source of attosecond pulses for a future beamline (cf. Sec. 2.2.1). In addition, the main factors influencing the conversion efficiency and the spectrum of the harmonic radiation are discussed theoretically (cf. Sec. 2.1.2) as well as experimentally (cf. Sec. 2.2.2). Furthermore, a method for isolating single attosecond pulses from the generated train of pulses is presented (cf. Sec. 2.1.1).

Currently it is possible to produce isolated attosecond pulses with durations as short as 43 as [5]. This allows to study many processes in chemistry, biology and physics on the most fundamental level by measuring the dynamics of the electrons involved. For example attosecond technology can be used to gain an understanding of charge transfer dynamics in semiconductors which could pave the way for optical computing [6]. Another field that is being explored are numerous biochemical reactions that are based on the transfer of electrons such as photosynthesis and the respiratory chain [7, 8].

Most of the experiments in ultrafast physics employ two laser pulses which are focused onto the target with a variable time delay. While the first pump-pulse triggers the process to be investigated, the second probe-pulse is used to record a "film" of its subsequent dynamic evolution. To this end, it is necessary to split the femtosecond beam at some point in the setup. This turns out to be challenging because conventional beamsplitters for such a broad wavelength range are hardly available and need to be used with an additional recompression stage to compensate for the dispersion introduced by their material.

For this reason, the possibility of using a holey mirror as beam splitting device is explored in the second part of this thesis. It offers the advantage that broadband reflective coatings are readily available for mirrors and that the beam passing through its hole does not acquire any dispersion. In particular, the influence of diffraction effects introduced by the hole are studied with regard to the focusing properties of the two emerging beams (cf. Sec. 3.3). The analysis reveals that, for the beam parameters generally used in high intensity laser experiments, both beams can still be used for HHG if the focusing length for the transmitted beam is adapted to the hole size (cf. Sec. 3.4). Yet, if a choice is available one should preferentially choose the reflected annular beam because it provides a slightly larger focal volume at any given peak intensity.

Chapter 2

High harmonic generation (HHG)

High harmonic generation is a tool that can be adjusted by a variety of parameters. After providing a general introduction to the functional principle of HHG, this section addresses the main factors which affect the efficiency of this process converting high-intensity femtosecond laser radiation to ultrashort pulses with attosecond duration.

2.1 Theory of high harmonic generation

If an atom is exposed to an intense laser field whose strength is comparable to that of the core's Coulomb field, it emits high-order odd harmonics of the incident laser light. The underlying process can be explained by the semiclassical three-step model (cf. Sec. 2.1.1). In brief, the external electric field tunnel-ionizes the atom when it peaks, accelerates the freed electron and drives it back to the parent ion with which it recombines about three quarters of the laser cycle later and emits its excess energy as photon. Its frequency usually falls in the XUV (10 - 124 eV) or soft X-ray (124 eV - 12 keV) spectral range [9]. A characteristic harmonic spectrum contains a plateau region where the intensity stays rather constant over many orders followed by a sharp cutoff region.

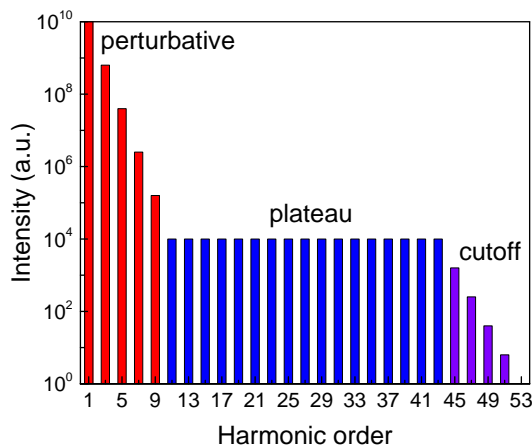


Figure 2.1: Schematic HHG spectrum. Low order harmonics can be explained by a perturbative theory (red) whereas the plateau (blue) and cutoff region (violet) require a description by non-perturbative theories like the three-step model.

In the temporal domain, high harmonic radiation appears as a train of coherent pulses with durations in the attosecond regime. These pulses are intrinsically synchronized to the generating laser field which make them an ideal tool to probe the ultrafast dynamics of electrons. Temporal resolutions of these measurements have been demonstrated to extend even to the sub-attosecond regime [10].

The generating process depends highly nonlinear on the intensity of the driving field and typically occurs at 10^{14} W/cm² - 10^{16} W/cm² for a wavelength of 800 nm [11]. It is usually implemented by focusing amplified femtosecond laser pulses on a gas target surrounded by high vacuum. The target can be a supersonic gas jet emerging from a small nozzle or a gas filled tube with two lateral holes for the laser beam to pass through. It has the size of a few mm and is backed by pressures ranging from about ten to several hundred millibars [12, 13]. Typically, noble gases like Helium, Neon or Argon are used given their high ionization energies. This is useful to prevent ionization of the gas by low intensity pre-pulses and to limit the amount of plasma generated by the main pulse (cf. Sec. 2.1.2).

Even under optimal conditions HHG remains a very unlikely process. At low laser repetition rates in the range of a few hertz to kilohertz 'high' conversion efficiencies of up to $\eta = 4 \cdot 10^{-5}$ for a specific harmonic order have been reported using Ti:sapphire lasers with pulse energies in the low millijoule range [14]. At higher repetition rates the pulse energy is lower which makes tighter focusing necessary. However, this aggravates the phase matching conditions of the nonlinear process leading to a reduced conversion efficiency (cf. Sec. 2.1.2). For example $\eta = 8 \cdot 10^{-6}$ has been achieved at 150 kHz repetition rate and $\eta = 5 \cdot 10^{-11}$ at 20 MHz [15, 16].

2.1.1 The three-step model

In contrast to HHG, low order nonlinear processes like second harmonic generation can be well described by a Taylor expansion of the polarization P induced in a medium by a strong electric field E :

$$P = \underbrace{\epsilon_0 \chi^{(1)} E}_{\text{linear polarization}} + \underbrace{\epsilon_0 \chi^{(2)} E^2 + \epsilon_0 \chi^{(3)} E^3 + \dots}_{\text{nonlinear polarization}} \quad (2.1)$$

where ϵ_0 is the vacuum permittivity and the nonlinear polarization response is regarded a small perturbation characterized by the optical susceptibilities $\chi^{(i)}$ with $i \geq 2$ [11].

However, this model fails to provide an accurate description of HHG - a process where the field strength cannot be regarded small anymore but approaches the level of an atom's Coulomb field. The first theory which could successfully explain the observed phenomena - especially the high frequency cutoff in harmonic spectra - was developed by Corkum in 1993 [17]. Since this semiclassical model provides an illustrative description of the process, it has been very successful and is known today as the three-step model.

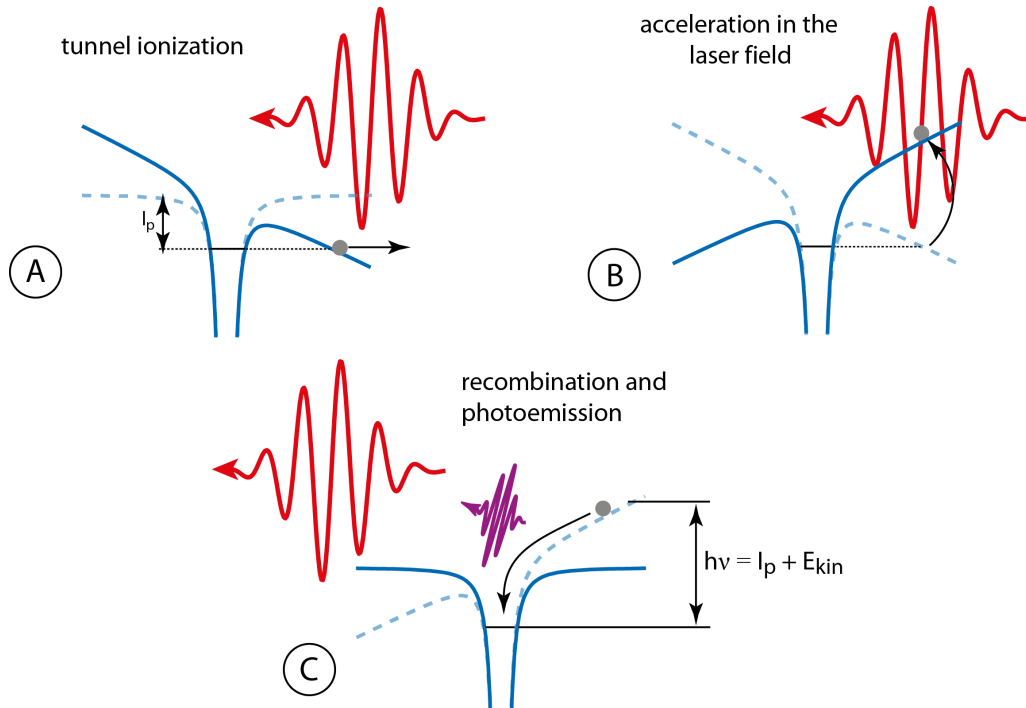


Figure 2.2: Three-step model for high harmonic generation. First, the strong electric field of a focused laser pulse (red, wavelength downscaled) substantially modifies the atomic potential (blue) during one of its peaks. This allows an outer shell electron to escape from the atom by tunneling through the lowered Coulomb barrier (**A**). Second, the released electron is accelerated in the external field and driven back to its parent ion which takes about three quarters of a laser cycle (**B**). Third, the electron recombines with the ion to its ground state by emitting a high energy photon (**C**). It contains the sum of the kinetic energy E_{kin} and the binding energy I_P . Figure is taken from Ref. [6].

Tunnel ionization

Tunnel ionization is a quantum mechanical phenomenon whose probability depends heavily on the length and height of a potential barrier. Only strong electric fields with intensities above approximately 10^{14} W/cm² are able to induce a sufficient lowering of the atomic Coulomb barrier to allow an electron to escape from it via this quantum path. The theory used by Corkum to describe this process is known as the **ADK model** developed by Ammosov, Delone, and Krařnov in 1986 [18].

It explains the intensity dependence of the tunnel ionization rate for an arbitrary initial quantum state of a neutral or an already ionized atom in an alternating electric field. The theory is based on the approximation that the tunneling time of the electron is much smaller than the oscillation period of the electric field. The result is an analytical formula

for the rate of ionization Γ_{ADK} :

$$\Gamma_{ADK} = \omega_s G_{lm} |C_{n^*l^*}|^2 \left(\frac{4\omega_s}{\omega_t} \right)^{2n^*-m-1} \exp\left(-\frac{4\omega_s}{3\omega_t}\right) \quad (2.2)$$

where $\omega_s = I_P/\hbar$ with the ionization potential I_P and $\omega_t = eE(2m_e I_P)^{-1/2}$ with the electric field amplitude E . G_{lm} and $C_{n^*l^*}$ are scaling factors depending on the initial state of the electron characterized by the (effective) azimuthal, magnetic and effective principal quantum numbers (l^*) l , m and n^* , respectively. The exact expressions can be obtained from Ref. [17]. As expected the tunnel ionization rate scales strongly with the intensity.

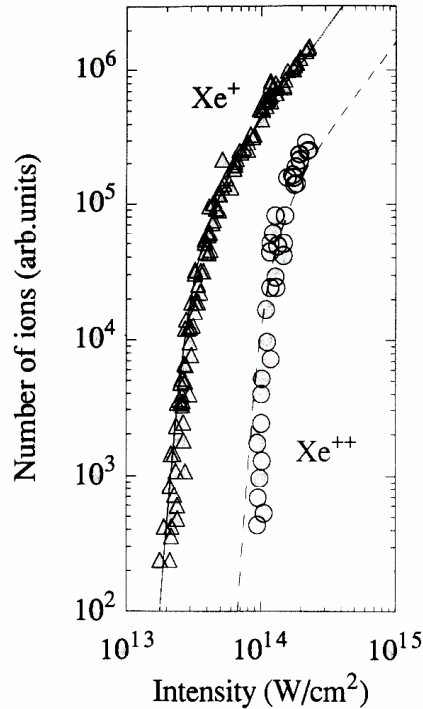


Figure 2.3: Intensity dependence of the ionization rate of Xenon for single and double ionization. The ADK formula (lines) is in very good agreement with the experimental values (symbols). Double ionized atoms can be neglected for HHG because the probability for this process is generally orders of magnitude lower for any given intensity. Figure is taken from Ref. [19].

In consequence, the electrons can only be released with a significant probability during a small period in time around one of the peaks of the external field. This results in the emission of a short bunch of electrons at each half-cycle of the driving laser field.

Acceleration in the laser field

For the next step, the electron is treated entirely classical. After the ionization process it can be approximated to be a free particle which is accelerated in the linearly polarized external field. Its motion is described by Newton's equation:

$$F = m_e \ddot{x}(t) = -eE_0 \cos(\omega_0 t) \quad (2.3)$$

where x is the position of the electron in polarization direction and F is the force exerted on it by an external field with field strength E_0 and carrier frequency ω_0 . For simplicity the intensity envelope is assumed to be constant corresponding to a many cycle pulse.

Assuming that the electron has zero velocity right after the tunneling process, its dynamic evolution can be obtained by integration. The corresponding initial conditions are $\dot{x}(t_0) = 0$ and $x(t_0) = 0$ where t_0 is the time when the electron is emitted.

$$\dot{x}(t) = -\frac{eE_0}{m_e \omega_0} (\sin(\omega_0 t) - \sin(\omega_0 t_0)) \quad (2.4)$$

$$x(t) = \frac{eE_0}{m_e \omega_0^2} (\cos(\omega_0 t) - \cos(\omega_0 t_0) + \omega_0(t - t_0) \sin(\omega_0 t_0)) \quad (2.5)$$

Depending on the time of emission, the electron may return to the ion at a later time t_{rec} . This translates into the condition $x(t_{rec}) \stackrel{!}{=} 0$. Inserting it into Eq. 2.5 yields a transcendental equation connecting the time of emission t_0 to the time of recombination t_{rec} that can be solved numerically. Looking at one half-cycle (i.e. $0 < \omega_0 t_0 < \pi$), solutions only exist if the electron is emitted within a quarter cycle after the peak of the electric field (i.e. $0 < \omega_0 t_0 < \pi/2$). In that case, the kinetic energy of the electron at the time of recombination can be calculated as:

$$E_{kin}(t_{rec}) = 2U_P (\sin(\omega_0 t_{rec}) - \sin(\omega_0 t_0))^2 \quad (2.6)$$

where $U_P = \frac{e^2 E_0^2}{4m_e \omega_0^2} \propto I_0 \lambda_0^2$ is the ponderomotive energy of the electron in the oscillating laser field with the peak intensity I_0 . The kinetic energy is maximal if the electron is emitted at a phase of 18° , i.e. slightly after the maximum of the electric field. The corresponding trajectory is referred to as the cutoff trajectory. Upon radiative recombination with the ion, it produces a photon with the highest achievable energy in the HHG spectrum. The photon carries the ionization energy I_P of the atom combined with the kinetic energy of the electron:

$$E_{max} = I_P + E_{kin} \approx I_P + 3.17 U_P$$

Photon energies below the cutoff can always be generated on two distinct trajectories referred to as the short and long trajectory. The short trajectory starts at a later time than the cutoff trajectory and recombines earlier whereas the long trajectory starts earlier and recombines later. The trajectory with the widest extent is the long trajectory starting out at 0° and returning at 360° , which spans a distance on the order of a few nanometers (2.6 nm at 10^{15} W/cm² and 780 nm). An example of electron trajectories is provided below in Fig. 2.4.

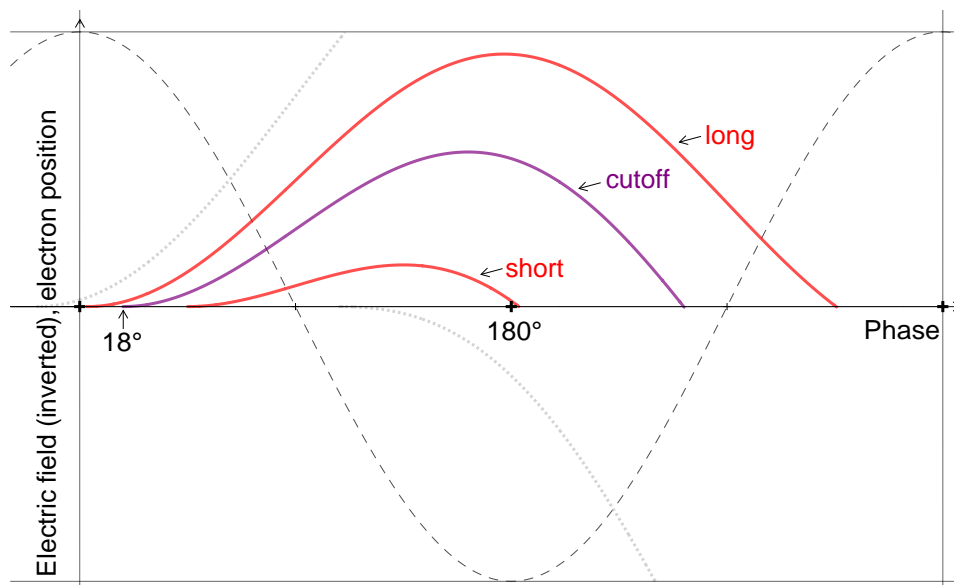


Figure 2.4: Electron trajectories in HHG. The cutoff trajectory with the highest possible kinetic energy starts at a phase of 18° after the peak of the external field and returns at a phase of 252° (violet). A short trajectory starting at 45° and the corresponding long trajectory starting at 3° yield the same return energy (red). Electrons emitted before the field peaks or after its first zero crossing will not return to the ion (gray dotted). The electric field of the laser is flipped horizontally for better display (black dashed).

Recombination and photoemission

If the electron returns to the ion, it may recombine radiatively generating a photon that carries its kinetic and binding energy. As outlined above, the energy depends strongly on the instant of time the electron is generated. For electrons propagating on short trajectories the return energy increases with the time of recombination corresponding to a positive chirp in the generated radiation. The opposite holds true for long trajectories. These features are visualized in Fig. 2.5 on the next page.

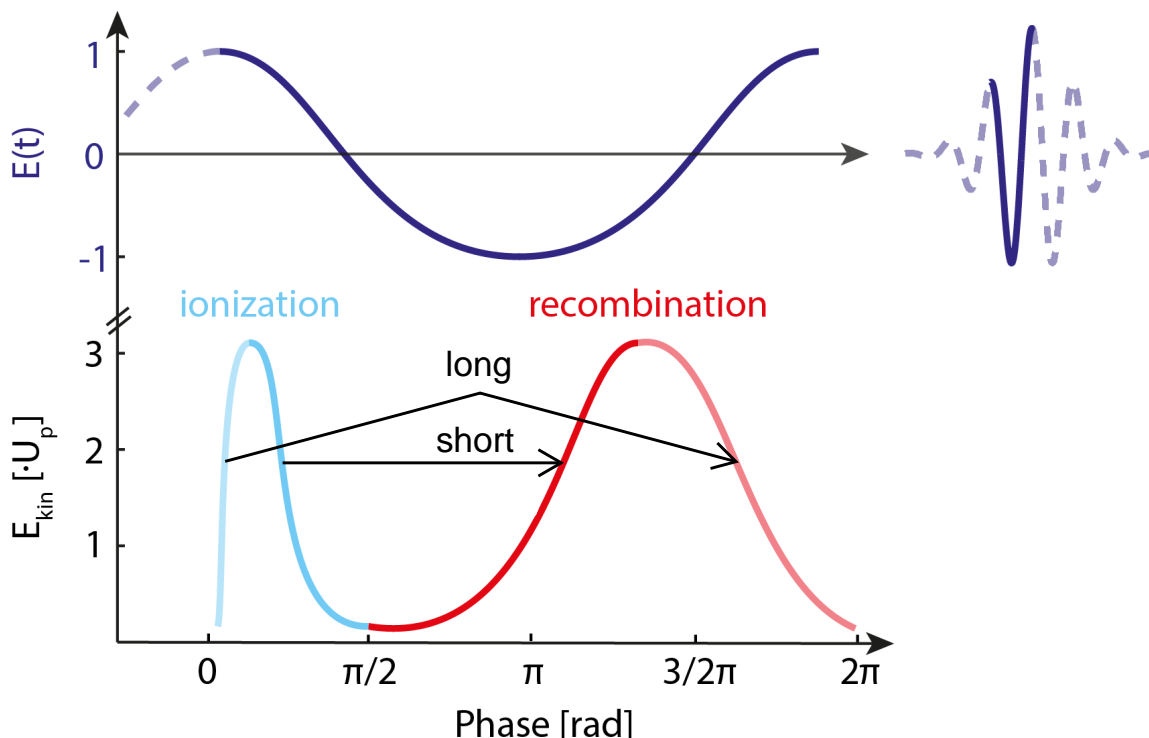


Figure 2.5: Return energy of electron trajectories. Electrons are tunnel-ionized close to a peak of the external field (dark blue). If they are emitted with a quarter cycle after the peak (light blue), they will return to the ion which happens during the rest of the cycle (red). The arrows depict the start and end point of a pair of short and long trajectories corresponding to the same return energy. Harmonic radiation originating from short trajectories carries a positive chirp (dark red) whereas long trajectories produce negatively chirped pulses (light red). Figure is adapted from Ref. [6].

In order to understand the characteristics of the harmonic spectrum, it is necessary to look at the combined response of many atoms over the full laser pulse duration. If it is sufficiently long, the electric field oscillates many times with almost the same amplitude. In that case, each half-cycle produces a burst of harmonic radiation with a similar spectral shape. The only main difference between adjacent bursts is their spectral phase which differs by two factors. Firstly it changes due to the shift in time domain which translates into a phase factor $\exp(i\omega T/2)$ in the spectral domain. In addition, there is a phase shift of π for monoatomic gases because due to their inversion symmetry adjacent half-cycles of the HHG process are exact mirror images of each other. This means that the electron's direction upon recombination alternates from half-cycle to half-cycle. Therefore, frequencies which are even multiples ($2n$) of the fundamental acquire a phase of $2n\omega_0 T_0/2 + \pi = (2n+1)\pi$ and interfere destructively. Hence, the resulting spectrum of the total pulse is modulated and contains only odd harmonics which interfere constructively. Deviations from this picture arise for high harmonics generated from molecules or surfaces [20].

This interference structure looks different if few or single cycle pulses are used where the strongest intensity peak of the electric field clearly dominates the other ones. Only electrons accelerated during this peak will generate the high frequency photons in the cutoff region of the harmonic spectrum. Under these circumstances, the cutoff remains unmodulated because there is no frequency contribution of another burst that could interfere with it. To illustrate this, the temporal structure of a train of attosecond pulses generated by a few-cycle pulse is depicted below in Fig. 2.6.

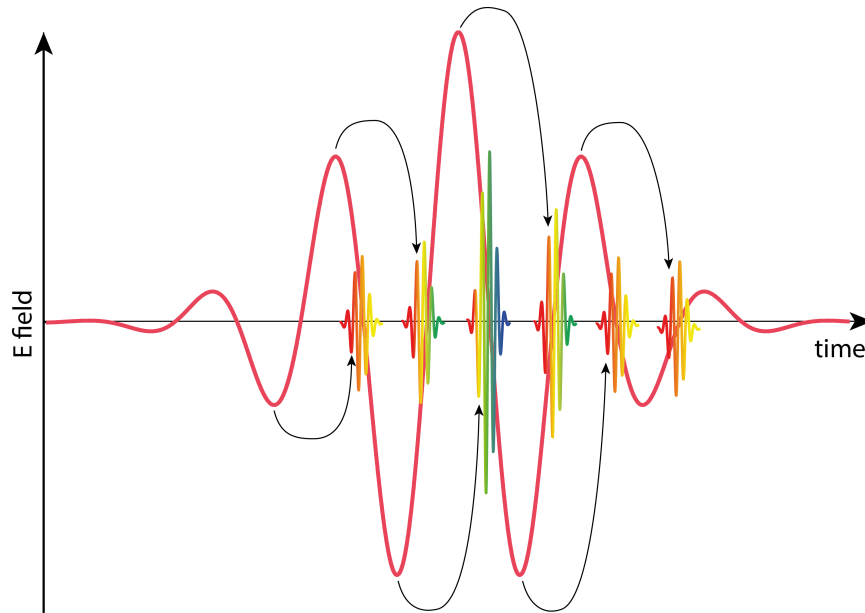


Figure 2.6: Emission characteristics of harmonic radiation. Free electrons are produced twice each cycle and gain energy in the laser field (red) while moving along their trajectories (black arrows indicate short trajectories). Upon recombination near the zero crossings of the field, short burst of harmonic radiation are generated. Their amplitudes depend on the number of electrons ionized at the beginning of the trajectory and thus change strongly with the peak intensity. Short trajectory harmonics are positively chirped which is visualized by the color gradient (low frequency: red, high frequency: blue). The varying intensity envelope of the generating field translates into different cutoff energies for the individual bursts. Hence, the highest frequency components are generated only once after the most intense half-cycle of the pulse. Figure is taken from Ref. [6].

For most experiments it is beneficial to isolate only one of these bursts in order to increase the temporal resolution. This can be accomplished by using bandpass mirrors or by sending the pulse train through a thin metal foil with a thickness of about a hundred nanometers to a few micrometers. The material can be chosen such that only the cutoff region of the harmonic spectrum is transmitted through it. Given that the cutoff is unmodulated, only the one burst attributed to it can pass this filter.

Another beneficial aspect of metal filters is that they usually impose a negative group delay dispersion onto the radiation passing through them [21]. In that way they can partly compensate for the intrinsic positive chirp of the short trajectory harmonics which compresses the pulses temporally. This method can be combined with other gating techniques which modify the driving field such that high harmonics are generated only during one half cycle [22]. In this way, the **generation of isolated attosecond pulses** with durations as short as 43 as could be demonstrated [5].

Based on the three-step model, a **fully quantum theory of HHG** was developed by Lewenstein in 1994 which yields a similar formula for the cutoff energy [23]. An interesting addition is the quantum description of the propagation of the free electron. Unlike electromagnetic waves, the electronic wave packet disperses in vacuum which reduces the recombination probability the longer the electron can spread during its propagation [24]. This explains two phenomena. First of all, it is advisable to adjust the generation process for a given harmonic energy to the short trajectory since it yields a higher output than the corresponding long trajectory with the same energy. In addition, the harmonic intensity I_{HHG} reduces strongly with increasing laser wavelength λ_0 because, in that case, the electron excursions are longer in time [25]:

$$I_{HHG} \propto \lambda_0^{-5.5 \pm 0.5}$$

However, it is important to note that photoemission is not the only process that can occur when the electron returns to its parent ion. Competing processes are [26]:

- **Above-threshold ionization (ATI)**

The electron scatters elastically with the ion. Although the electron keeps most of its energy in this process, the interaction with the atom is necessary to mediate both momentum and energy conversion in the photon absorption process. The emerging electron spectra show peaks which are spaced by once the fundamental frequency only. This is due to the fact that electrons emerging from two neighboring peaks will leave the atom in different directions after recombination and thus cannot interfere with each other substantially.

- **Non-sequential double ionization**

The electron scatters inelastically with the ion. If a sufficient amount of energy is transferred to another bound electron, it is ejected as well leaving behind a doubly ionized atom.

2.1.2 Optimizing the harmonic yield

In order to maximize the intensity of the harmonic radiation for a given order, it is necessary to understand the interplay between the experimental accessible parameters of the HHG process. An overview of the main influencing factors is provided in this section.

Phase matching

Like other nonlinear optical processes, HHG can only be efficient when the fundamental wave is phase matched to the generated harmonics. This is based on the fact that the nonlinear process can take place at different locations along the propagation direction and the phase velocity of the fundamental wave is in general different from that of the product wave. Only if the generated photons all leave the interaction zone with the same phase, regardless of their origin position, they can interfere constructively to form the harmonic radiation.

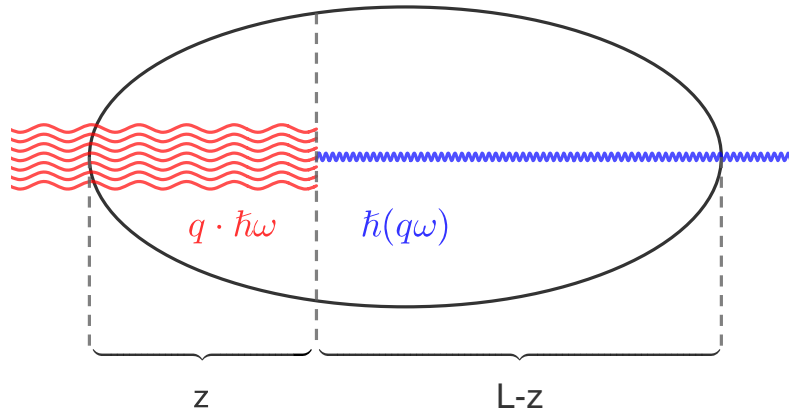


Figure 2.7: Phase matching in HHG. z is the interaction point which is located at an arbitrary position within the focal volume of length L formed by a laser with carrier frequency ω_0 . The generation of the q^{th} harmonic is phase matched if the phase of the generated harmonic photon is independent of its origin z .

Mathematically, this condition can be expressed by requiring that the total phase of the generated photon $\phi_{total} = q\phi_{\omega_0}(z) + \phi_{q\omega_0}(L - z) = (qk_{\omega_0} - k_{q\omega_0})z + Lk_{q\omega_0}$ ¹ is independent of z . This yields the **phase matching condition**:

$$\Delta k = qk_{\omega_0} - k_{q\omega_0} \stackrel{!}{=} 0$$

¹The second equivalence holds if the phase is linear: $\phi = zk$ where k is the absolute value of the wave vector.

For HHG there are mainly four contributions which cause phase mismatch that will be analyzed in the following.

One source of phase mismatch, which is common for all nonlinear processes, is the **atomic dispersion**. It occurs due to the wavelength dependence of the refractive index n of the generating medium resulting in different optical path lengths for the fundamental and the harmonic wave. For the commonly used noble gases the difference ($n_{\omega_0} - n_{q\omega_0}$) is positive and takes on a value ranging between $3 \cdot 10^{-4}$ and $4 \cdot 10^{-4}$ at a fundamental wavelength of $\lambda_0 = 800$ nm for harmonics with $q > 21$ at standard conditions (1013 mbar, 273 K) [27]. As a consequence, the effect of atomic dispersion is rather small for HHG from noble gases.

Due to the high intensity of the fundamental wave, a fraction η of the atoms will be ionized. The resulting ions have a low polarizability and thus their dispersion can be neglected. On the other hand, the interaction between the **free electrons** and the electric field depends strongly on the wavelength and can be described by the refractive index of a plasma:

$$n(\omega) = \sqrt{1 - \frac{\omega_P^2}{\omega^2}} = \sqrt{1 - \frac{N_e e^2}{\epsilon_0 m_e \omega^2}} \approx 1 - \frac{N_e e^2}{2\epsilon_0 m_e \omega^2} \quad (2.7)$$

where N_e is the number density of free electrons and the approximation is valid if the frequency of the radiation ω is much larger than the plasma frequency ω_P , which is usually the case for the low density plasmas generated in gases. Unlike in case of atomic dispersion, the difference in refractive indices is negative for electronic dispersion such that these effects can partly compensate each other.

A third contribution is caused by the geometry of the focal volume. For a Gaussian beam the effect is described by the **Gouy phase**, a propagation phase which changes its sign in the focal plane:

$$\phi_{Gouy}(\omega, z) = -\tan^{-1}\left(\frac{z}{z_R}\right) = -\tan^{-1}\left(\frac{2cz}{\omega w_0^2}\right) \quad (2.8)$$

where w_0 is the size of the focal beam waist. Since the Rayleigh length z_R rises proportionally to ω , the Gouy phase of the high harmonic beam changes only weakly in the focal volume compared to the fundamental beam and can be neglected. In addition, HHG occurs only in a limited part of the focal volume. Therefore, the formula can be linearized around the point z_0 where the generation probability is highest:

$$\begin{aligned} \phi_{Gouy,q} &= q \underbrace{\phi_{Gouy}(\omega_0, z)}_{\text{fundamental beam}} - \underbrace{\frac{\pi}{2} - \phi_{Gouy}(q\omega_0, z)}_{\text{high harmonic beam}} \\ &\approx \phi_0 + q(z - z_0) \left. \frac{\partial \phi_{Gouy}(q\omega_0, z)}{\partial z} \right|_{z=z_0} \\ &= \phi_0 - q(z - z_0) \frac{z_R}{z_R^2 + z_0^2} \end{aligned} \quad (2.9)$$

It is useful to define the coherence length L_{Gouy} by requiring that the Gouy phase changes by less than π over this length [27]:

$$L_{Gouy} = \frac{\pi}{q} \frac{z_R^2 + z_0^2}{z_R} \quad (2.10)$$

For a typical setup² generating harmonics close to the beam center $z_0 = 0$, it takes on a value of 0.45 mm. In general, the coherence length can be increased by displacing the gas target from the focus of the fundamental beam. This increases the efficiency of the harmonic generation while at the same time reducing the intensity envelope of the generating field. So a maximal output can be expected at an intermediate distance. However, for a deeper examination of this effect, it is necessary to note that the Gouy phase also causes a spatial variation of the carrier-envelope phase (cf. Sec. 2.2.3) in the vicinity of the focus. This effect plays an important role when using few-cycle pulses and has been verified experimentally [28].

An additional cause of phase mismatch arises due the action that the electronic wave packet acquires along its trajectory before recombining with the atom. This quantum mechanical effect has been studied by Lewenstein and L’Huillier and is referred to as **dipole phase** [29]. To a first approximation it is proportional to the duration τ of a given trajectory and depends linearly on the intensity:

$$\phi_{Dipole} \approx -\tau U_P \approx -\alpha I \quad (2.11)$$

where the value of α is determined by the considered trajectory. For the single trajectory in the cutoff region a value of $\alpha_{Cutoff} \approx 13.7 \cdot 10^{-14}$ rad cm²/W could be determined. In the plateau region short and long trajectories coexist which are characterized by $\alpha_{short} \approx 1.4 \cdot 10^{-14}$ rad cm²/W and $\alpha_{long} \approx 25.7 \cdot 10^{-14}$ rad cm²/W [3].

Since the intensity depends on the longitudinal and radial position in the focal volume, the dipole phase is mainly responsible for the mode structure of the generated harmonic beam. If all other parameters are adjusted, the phase matching condition picks out the positions in the focal volume where the intensity has the right value for the dipole phase to cancel out the remaining phase contributions. In that way the phase matching can either be fulfilled on axis forming a round beam or off axis producing an annular beam structure.

²The laser is assumed to generate the 25th order harmonic at a central wavelength of $\lambda_0 = 780$ nm with 1/e field width of $w_0 = 5$ mm focused over a length of 60 cm.

In summary, the **complete phase matching condition for HHG** reads:³

$$\Delta k_q = \underbrace{\frac{q\omega_0}{c} P (1 - \eta) (n_{\omega_0} - n_{q\omega_0})}_{\text{atomic dispersion (+)}} - \underbrace{\frac{P\eta}{\omega_0} \frac{q^2 - 1}{q} \frac{N_{at}e^2}{2\epsilon_0 m_e c}}_{\text{electronic dispersion (-)}} - \underbrace{q \frac{z_R}{z_R^2 + z_0^2}}_{\text{Gouy phase (-)}} - \underbrace{\alpha \frac{\partial I}{\partial z} \Big|_{z=z_0}}_{\text{dipole phase (+)}} \stackrel{!}{=} 0$$

where P is the pressure of the gas target, ω_0 is the fundamental laser frequency, q is the harmonic order, η is the fraction of ionized atoms, n_ω is the refractive index of the medium per unit pressure at frequency ω , N_{at} is the atomic number density per pressure, z_R is the Rayleigh length of the fundamental beam at the focal waist, I is its intensity and α is a constant labeling a given trajectory. The sign shows which contributions may cancel out. Since the dipole phase is proportional to the gradient of the intensity, its sign depends on the position of the focus relative to the gas target.

Thus, to optimize the phase matching for a given harmonic order, many parameters are experimentally available. Changing the **pressure** of the gas target results in a different ratio of atomic and electronic dispersion. Raising the **intensity** of the fundamental beam increases the influence of the dipole phase and the electronic dispersion due to higher ionization. It also affects the atomic dispersion because the refractive index carries an intensity dependence that is not negligible for the fundamental beam. The **size of the focus** w_0 **and its position** z_0 relative to the gas target have an influence on all the parameters because they modify the intensity, the Rayleigh length $z_R(w_0)$ and the Gouy and dipole phase as explained above.

If the phase matching condition was met in every position of the focus, the field of all the emitting atoms would add up constructively yielding a harmonic intensity that rises quadratically with the focal volume. However, this situation can not be achieved - essentially because the intensity of the driving wave is not homogeneously distributed over the focal volume. Only as long as the phase mismatch is smaller than π , the generated photons can interfere constructively. This condition is met over a coherence length $L_C = \pi/\Delta k_q$ which can be used as a measure of the degree of phase matching. As a general rule, the coherence length is longer in loose focusing conditions⁴ because the intensity gradient in the focal volume is lower in that case. This leads to higher conversion efficiencies at the expense of the intensity of the driving field.

³In order to compare the Gouy phase mismatch to the wave vector mismatch, it was assumed that the harmonics are generated near the center of the focus, i.e. $z_0 \approx 0$.

⁴In this context, loose focusing means using focal lengths on the order of 1 m which generates long focal spots on the order of a few millimeters.

Reabsorption

Unfortunately the generated photons fall in a spectral range where most materials absorb radiation strongly - including the medium used for their generation. The transmission through the gas decreases exponentially with the medium length L_{med} on the scale of the absorption length $L_{abs} = 1/(\sigma\rho)$ where σ is the (wavelength dependent) ionization cross section of the gas and ρ its density:

$$T = \exp\left(-\frac{L_{med}}{L_{abs}}\right) \quad (2.12)$$

Especially the intermediate order harmonics are affected by reabsorption because the typically used noble gases He, Ne and Ar absorb strongly in this frequency range as can be seen below in Fig. 2.8.

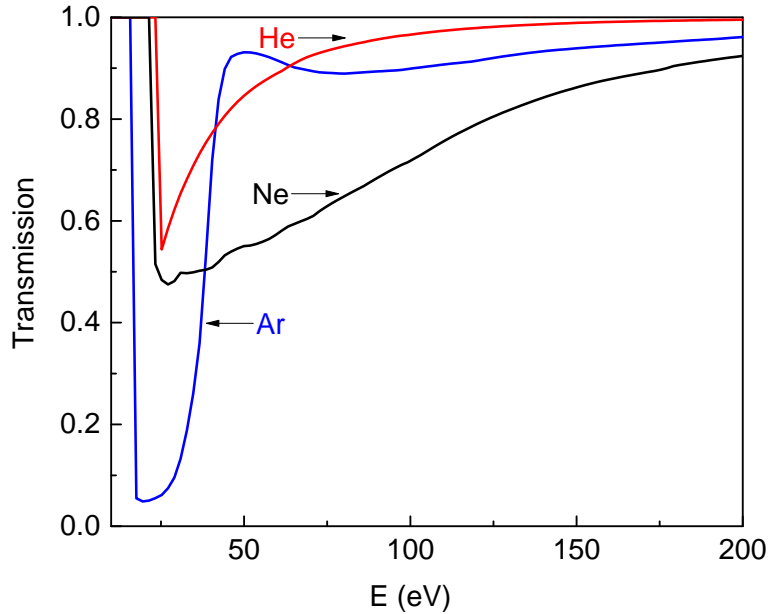


Figure 2.8: XUV transmission for noble gas targets with length 3 mm at a pressure of 10 mbar. Note that the transmission drops exponentially with increasing pressure and medium length. The dip in transmission occurs due to resonant ionization of the gases at 24.6 eV, 21.6 eV and 15.8 eV for He, Ne and Ar, respectively [30]. Transmission data is taken from Henke [31].

So even if good phase matching is achieved at high particle densities over a large coherence length, the harmonic yield will eventually peak at a certain pressure and target length due to the **reabsorption limit**. The interplay of these effects has been studied both experimentally and theoretically by Constant et al. [14].

Ellipticity and relativistic limit

The crucial step in HHG is the recombination of the accelerated electronic wave packet with the parent ion. This process depends heavily on the form of the electron's trajectory. If the driving field is not linearly polarized but exhibits a small **ellipticity**, the electron will miss the ion on its way back. A calculation based on first order perturbation theory predicts an exponentially decreasing harmonic yield which has been experimentally verified for a wide range of intensities and target gases [32]. The results are presented below in Fig. 2.9.

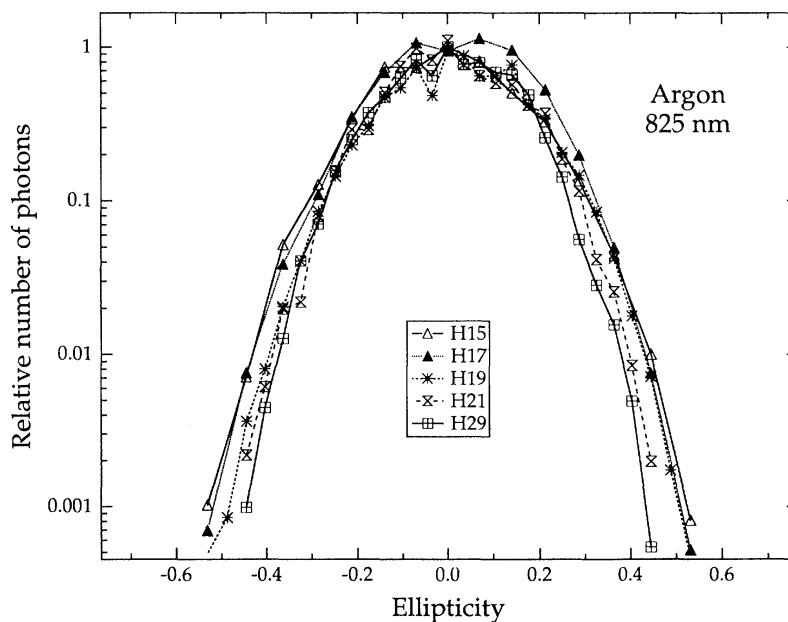


Figure 2.9: Influence of driving field ellipticity on the harmonic yield. Harmonics of the order indicated in the figure are produced in Argon at an intensity of $4 \cdot 10^{14} \text{ W/cm}^2$ at 825 nm. Experimental results (symbols) are normalized and compared to first order perturbation theory (lines). Figure is taken from Ref. [32].

Another issue arises when the laser intensity approaches the **relativistic limit** at about 10^{17} W/cm^2 for 800 nm. Above this intensity, the magnetic component of the driving field is not negligible anymore and the resulting Lorentz force deviates the electron from its linear trajectory which makes it miss the ion. However, this limitation can be overcome by assisting the driving laser with a weak attosecond pulse train which compensates the additional force. This technique has been applied successfully to generate harmonics up to the MeV range [33].

Plasma defocusing and ionization

Ionization results in the buildup of a **plasma** in the focal volume as discussed in Sec. 2.1.2. Since the amount of ionization is linked to the intensity, the plasma density is highest on axis and drops off radially. Now the plasma's refractive index is always less than one and thus below that of the gas target. So the total refractive index is lowest on axis and increases towards the wings of the beam. This can be thought of as a **defocusing lens** whose effect increases with pressure, length of the gas target and intensity [34]. As a consequence, the beam diverges which reduces the size of the focus and its maximal intensity. This effect is mainly responsible for the pressure dependence of the harmonic yield. For low order harmonics the number of generated photons increases with pressure (up to the absorption limit) because the density of emitters is increased. On the other hand, the conversion efficiency for the high order harmonics drops off rapidly with increasing pressure because their yield depends strongly on the maximal intensity [35]. This effectively shifts the spectrum to lower energies and is in good agreement with theoretical predictions presented below in Fig. 2.10.

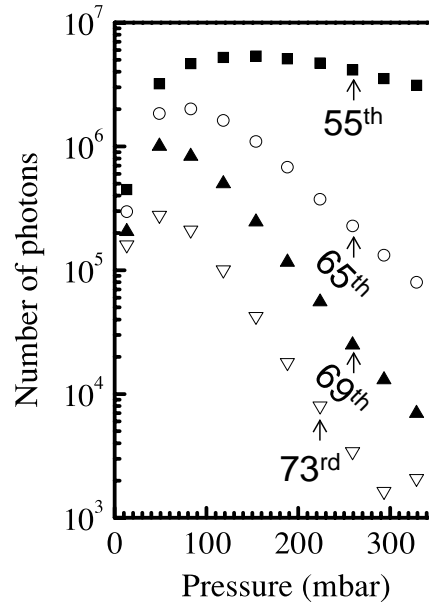


Figure 2.10: Calculated pressure dependence of the harmonic yield taking plasma defocusing into account. The number of generated photons increases with pressure for harmonics in the plateau region (55th) and decreases for high order harmonics (65th, 69th, 73rd). The length of the gas target is 3 mm and the peak intensity is $8 \cdot 10^{14} \text{ W/cm}^2$. The values agree well with the experimental study. Figure is taken from Ref. [34].

Another ionization related problem is that the phase matching condition described in Sec. 2.1.2 cannot be fulfilled for arbitrarily high levels of ionization because at some point, the negative contribution of the electronic dispersion cannot be compensated for anymore. As a rough estimate, neglecting the Gouy and dipole phase, one can define

a **critical ionization fraction** at which the atomic dispersion just compensates for the electronic dispersion:

$$\eta_{crit} = \left(1 + \frac{N_{at}e^2}{2\epsilon_0 m_e} \frac{1}{(n_{\omega_0} - n_{q\omega_0}) w_0^2} \right)^{-1} \quad (2.13)$$

Using intensities which lead to higher ionization levels causes increased phase mismatch and thus reduce the conversion efficiency. Typical critical levels of ionization at 800 nm are about 4 %, 1 % and 0.5 % for Ar, Ne and He, respectively, which translates to a cutoff energy of 50, 90 and 130 eV, respectively [36]. Increasing the wavelength lowers the critical ionization fraction scaling approximately as $\eta_{crit} \propto \lambda_0^{-2}$. Fortunately a slight decrease in intensity is already enough to lower the ionization rate sufficiently. As a consequence, the cutoff energy for a single atom scaling approximately as $E_{cutoff} \propto \lambda_0^2$ is only changed modestly. Calculations for the mid-IR wavelength range (0.8 – 10 μm) along with experimental data suggest that the **scaling law for the harmonic cutoff** is changed to [36]:

$$E_{cutoff} \propto \lambda_0^{1.65 \pm 0.05}$$

To overcome this limitation, it is possible to employ **quasi phase matching** techniques, i.e. using a gas filled waveguide whose diameter is periodically modulated. Only in its narrow regions the laser intensity is high enough for HHG to occur. In between these sections the laser light rephases with the generated harmonic radiation, so that the the subsequently generated photons always contribute in phase to the existing beam. This technique has been used successfully to increase both the cutoff energy and the photon flux [37].

2.2 Experimental implementation of HHG

In the course of this work, we designed and commissioned a setup for HHG which will be used as a source of attosecond pulses in a future beamline. In addition, the generated radiation was characterized spectrally with regards to its dependence on the target gas pressure and the CE phase of the driving field. The experimental results are presented in this section.

2.2.1 Laser setup

Fig. 2.11 shows the setup used for the generation and spectral analysis of high harmonic radiation. First of all, femtosecond few-cycle laser pulses centered at 780 nm are produced using the FP2 laser system located in the Laboratory for Attosecond Physics at the Max-Planck Institute for Quantum Optics. Its basis is a Ti:Sapphire oscillator generating pulses with a spectral width corresponding to a transform limit of 6 fs and an energy of about 3 nJ at a repetition rate of 78 MHz [38].

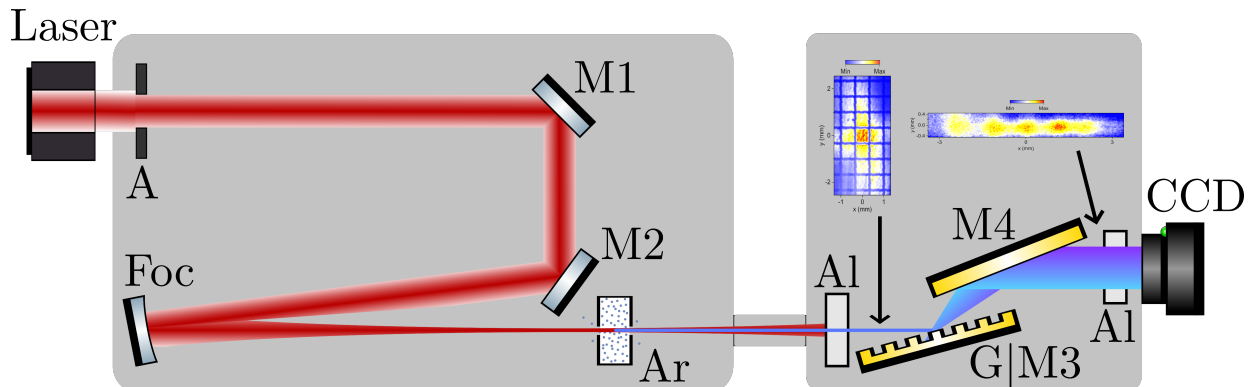


Figure 2.11: Experimental setup consisting of the HHG chamber (left) and the XUV spectrometer chamber (right). Abbreviations: red beam: fundamental, blue beam: harmonic (violet: high frequency, light blue: low frequency), A: motorized aperture, M1,M2,M3,M4: motorized mirrors coated with silver or gold, respectively (M1 will be replaced by a beam-splitter for future pump-probe experiments), Foc: spherical mirror (focal length = 60 cm), Ar: gas target filled with argon, Al: 0.5 μm aluminum filter, G: gold coated grating (can be replaced by M3 via a motorized translation stage), CCD: XUV camera, insets: harmonic beam profile (left), spectrum (right).

In the next step, the carrier-envelope phase (CEP) of the pulses is measured via f-to-zero interferometry based on difference frequency generation between the oscillator modes in a periodically poled MgO doped lithium niobate (PP-MgO:LN) crystal [39]. The resulting signal is used in a fast feed-forward loop to adjust an acousto-optic frequency shifter (AOFS) placed behind the oscillator. It subtracts the frequency of an acoustic phonon from all the lines of the pulses' comb spectrum, thereby setting their offset to zero. In this way pulse to pulse fluctuations in the CE phase are removed [40].

Subsequently the pulses are sent to a nine-pass chirped pulse amplifier (CPA) which increases their energy to 900 μJ . It consists of a thick glass block to stretch the pulses to a duration of several picoseconds, the Ti:Sapphire amplifier medium pumped by a pulsed Nd:YLF laser and a Pockels cell combined with a polarizer which picks out every $\sim 26.000^{\text{th}}$ pulse thereby reducing the repetition rate to 3 kHz. Furthermore, an acousto-optic modulator (Dazzler) is used for spectral shaping and higher order dispersion control which allows for the use of a transmission grating compressor for the temporal recompression of the pulses [6].

In the next step the amplified pulses are focused into a hollow-core fiber (HCF) with 250 μm core diameter and a length of one meter. It is filled with Neon at a pressure of 1.6 bar. The nonlinear interaction with the gas leads to self phase modulation and self steepening of the pulses resulting in strong spectral broadening. Right after the fiber, the CE phase is measured again via f-to-2f interferometry and the resulting beat signal is

passed on to a slow feedback loop which regulates the thickness of a piezo prism in front of the CPA [39]. This allows to correct CE phase fluctuations arising from environmental instabilities when the pulses pass through the CPA and the HCF.

Before the beam is sent to the experiment in a vacuum chamber, a four-pair double-angle chirped mirror compressor is used to remove and precompensate additional dispersion introduced by the glass windows of the fiber, the propagation through air and the vacuum window. For fine tuning of the dispersion, a pair of movable SiO₂ wedges is used which allows to adjust the amount of material dispersion in the beam path. In this way we generate nearly transform limited pulses with an octave spanning spectrum and a pulse energy of about 400 μ J.

The gas target consists of a small tube with two lateral holes for the laser beam to pass through. It is filled with Argon at a backing pressure of 40 to 60 mbar and is surrounded by a vacuum on the order of 10^{-3} mbar maintained by a turbomolecular pump. To generate high harmonics, we loosely focused the laser pulses onto the target by means of a spherical mirror with a focal length of 60 cm. In order to adjust the position of the target relative to the focus, it is positioned on a motorized 3D translation stage. Furthermore, two motorized mirrors (M2, Foc) are used to steer the direction of the beam. Following the generation process, both the remaining fundamental light and the high harmonics propagate collinearly into the second vacuum chamber. Here, the fundamental beam is blocked by a thin 0.5 μ m aluminum filter which is transmissive only for the high frequency harmonic beam.

For spectral measurements we assembled an XUV spectrometer in the second vacuum chamber. All optics in this chamber carry an unprotected gold coating and are placed at large incidence angles ($> 70^\circ$) to maximize reflection of the XUV radiation. The spectrometer consists of a toroidal gold grating (groove density = 450/mm) mounted on a 1D translation stage and a motorized mirror which is used to steer the dispersed beam onto an XUV camera. To protect the camera from scattered light of the high intensity fundamental beam, we mounted another 0.5 μ m aluminum filter right in front of the CCD chip.

As a first step, we optimized the overall intensity of the harmonic beam. To this end, another mirror (M4) also mounted on the translation stage can be moved in the beam path, which allows to observe the mode structure of the harmonic beam. Several parameters can be varied to achieve optimal phase matching. First of all, the focal intensity was tuned by adjusting a motorized iris placed in the beam path at the entrance to the HHG chamber. Furthermore, the position and pressure of the gas target can be modified. Besides that, changing the amount of dispersion by moving the wedges in the final recompression stage provides control of the pulse duration. Optimal conditions were reached at a pressure of 60 mbar and an amount of dispersion which provides maximal recompression of the pulse. We used these settings as a basis to study the dependence of the harmonic spectrum on the gas pressure and the carrier-envelope phase of the laser pulse.

2.2.2 Pressure dependence of HHG

We calibrated the measured XUV spectra by using the known transmission of the aluminum filter given below in Fig. 2.12:

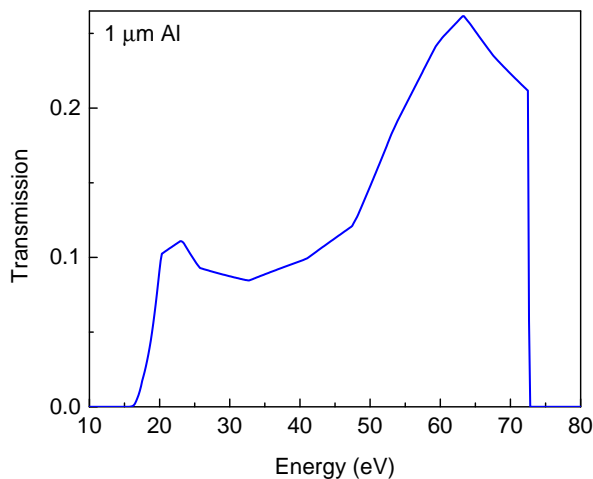


Figure 2.12: XUV transmission of a 1 μm aluminum filter. Data is taken from Henke [31].

Aluminum only transmits radiation in an energy window of 16.5 eV to 72.6 eV which is delimited by a clear cutoff. At least one of these edges should be visible in XUV spectra with a sufficiently broad bandwidth. Here, the high energy edge at 72.6 eV is used for the calibration combined with the spacing of the odd harmonic peaks which is 3.2 eV for a driver wavelength of 780 nm. The results are presented below in Fig. 2.13.

As expected from theory, the HHG spectrum shifts to higher energies when reducing the pressure (Fig. 2.13). This can be explained by a reduced plasma density which is beneficial for the generation of higher order harmonics (cf. Sec. 2.1.2). At the same time, the harmonic peaks nearly keep their position which is in agreement with the three-step model (cf. Sec. 2.1.1). When good phase matching is achieved in the observed spectral range the typical plateau like structure of the harmonic spectrum becomes apparent (50 mbar - 60 mbar).

The fact that we could not observe a clear cutoff as expected from the filter transmission data is attributed to a non-ideal positioning of the grating. Its focusing properties are tailored for being used in combination with a toroidal mirror in a later stage of the experiment. With the present setup however, the XUV camera needs to be placed after the focal plane of the grating for reasons of space. As a consequence, it is only possible to observe the spectrum convolved with a scaled version of the spatial mode profile. This leads to the disappearance of sharp feature in the recorded intensity distributions.

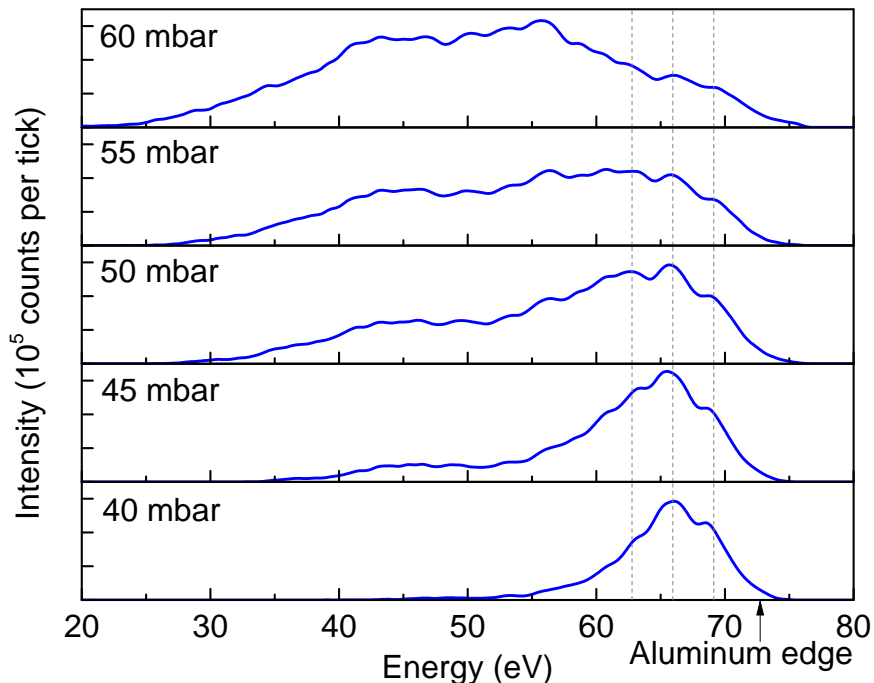


Figure 2.13: Target pressure dependence of HHG in Argon. Spectra were measured for different backing pressures of the gas target after transmission through a 1 μm aluminum filter. The energy axis is scaled according to the distance of the harmonic peaks and its offset is based on the estimated position of the high energy cutoff of the filter at 72.6 eV (arrow). Parts of the spectrum above this energy are attributed to an overlap effect because the XUV camera was not positioned in the focal plane of the grating. As an example, the gray dotted lines indicate three peaks that are visible in all spectra. The spectrally varying filter transmission (Fig. 2.12) has been subtracted.

2.2.3 Carrier-envelope phase (CEP) dependence of HHG

The carrier-envelope phase describes the phase offset ϕ_0 between the carrier of a pulse oscillating with frequency ω_0 and its slowly varying envelope. For example, the electric field of a Gaussian pulse with duration T and CE offset ϕ_0 can be described in the following form:

$$E = \cos(\omega_0 t + \phi_0) \exp\left(-\frac{t^2}{T^2}\right) \quad (2.14)$$

A change in the CE phase leaves many cycle pulses almost unaffected because their envelope is nearly constant within one cycle duration. However, for pulses with a cycle duration approaching the pulse duration their shape is largely affected by the CE phase. Some examples are given on the next page in Fig. 2.14.

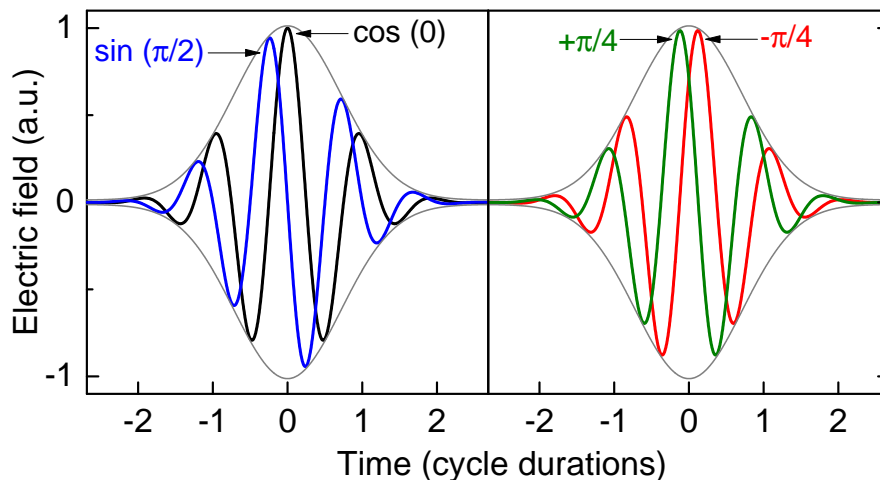


Figure 2.14: CEP of a few-cycle pulse. For a sine waveform ($\text{CEP} = \pi/2$, blue on the left panel) each peak of the electric field at negative times has a corresponding peak at positive times with the same intensity. This symmetry is broken for a cosine waveform ($\text{CEP} = 0$, black on the left panel). Here, the peaks form pairs with the same amplitude except for the most intense one in the center of the pulse. A pulse with CE phase $+\pi/4$ is the same as a pulse with CE phase $-\pi/4$ mirrored on the amplitude axis at time zero. The only difference is the order of their peaks. For the $-\pi/4$ pulse the peaks before the maximum have a higher amplitude than the ones after the maximum. The opposite is true for the $+\pi/4$ pulse. A CE phase shift of π does not change the intensity profile of the pulse.

Since HHG depends critically on the peak intensities of the electric field, a modification in CE phase changes the spectral characteristics of the harmonic radiation. To observe this effect we varied the CE phase of the driving pulse in steps of 0.3 rad with the gas pressure fixed at the previously found optimum of 60 mbar. This is achieved by adjusting the amount of material in the beam path with the piezo prism controlled by the slow loop of the CEP stabilization scheme (cf. Sec. 2.2.1). At first, the results for a pulse with increased pulse duration are presented on the next page in Fig. 2.15. The temporal broadening is realized by manually shifting the wedges in the final recompression stage out of their optimal position, which adds material dispersion to the electric field.

The spectrum shows significant modulations indicating that the pulse consists of several half-cycles whose contributions to the harmonic radiation interfere with each other. However, the pulse is still sufficiently short for the CEP to have an impact on the spectrum. Since the central peak of the driving pulse has the highest intensity for a cosine waveform, it generates the highest cutoff energy of all waveforms. So we identify the spectrum in the upper panel to be generated by a cosine waveform. Changing the CEP by $\pi/2$ results in a sine waveform. For a Gaussian pulse, this waveform is expected to show deeper spectral modulations because all peak intensities occur in pairs which enhances the interference. However, we observed the opposite which means that the pulse envelope is distorted due to the higher order dispersion effects of the wedges used for the temporal broadening.

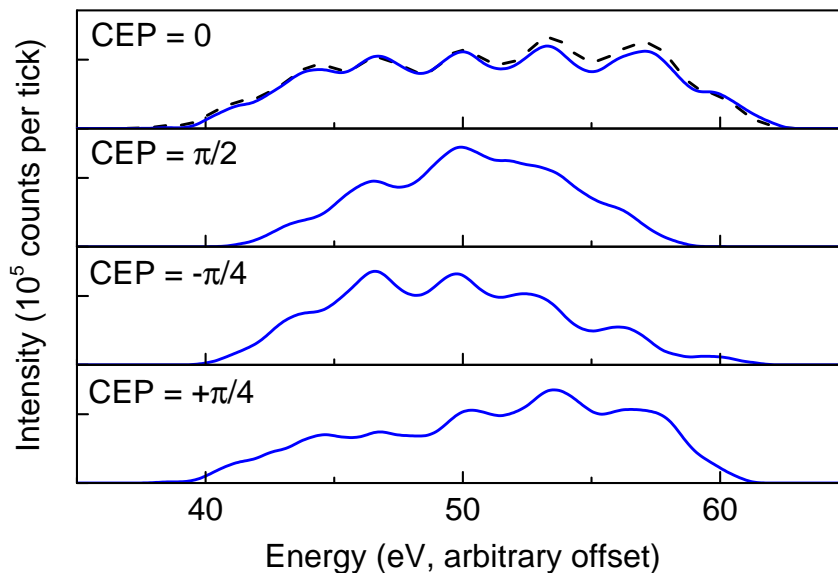


Figure 2.15: CEP dependence of HHG for few-cycle pulse with added dispersion. The difference in CE phase is adjusted with a precision of 0.15 rad whereas the identification with the absolute phase values is explained in the text. The black dashed line in the upper panel corresponds to a CE phase of π which nearly reproduces the spectrum with a CE phase of 0 as expected. This proves that the CE phase stabilization works accurately. The energy axis has an arbitrary offset because the entire spectrum lies within the aluminum window of 16.5 eV to 72.6 eV. To make the photon count rates comparable to Figs. 2.13 and 2.16, the average transmission of the aluminum filter of 15 % has been subtracted [31].

An interesting observation can be made for a CE phase shift of $\pm\pi/4$ because these pulses have identical peak intensities (cf. Fig. 2.14). As a consequence, the spectra generated by them have the same high energy cutoff. However, since the peaks before the maximum have a higher amplitude for the $-\pi/4$ pulse more plasma will have been generated by the time the central peak produces the harmonics in the cutoff region. This has a negative effect on the phase matching for the harmonics with highest order and explains why their intensity is lower. The opposite holds true for the $+\pi/4$ pulse, for which less plasma is generated before the central peak and thus the efficiency for high energy harmonics is increased.

For the pulse without added dispersion, different spectral shapes arise (Fig. 2.16). Due to the higher intensity of the short pulse, the harmonic radiation has an about three times higher spectral intensity and covers a much larger energy range of about 55 eV compared to 20 eV for the long pulse. In addition, the interference structure in the spectra nearly vanishes for all values of the CE phase indicating that the pulse consists only of very few half-cycles [41]. Again, we identify the pulse producing the highest intensities in the cutoff of the spectrum to have a cosine waveform. Studying the two panels on the bottom, a shift to lower (higher) energies can be observed for the $-\pi/4$ ($+\pi/4$) pulse. However, the effect is less prominent than for the long pulse.

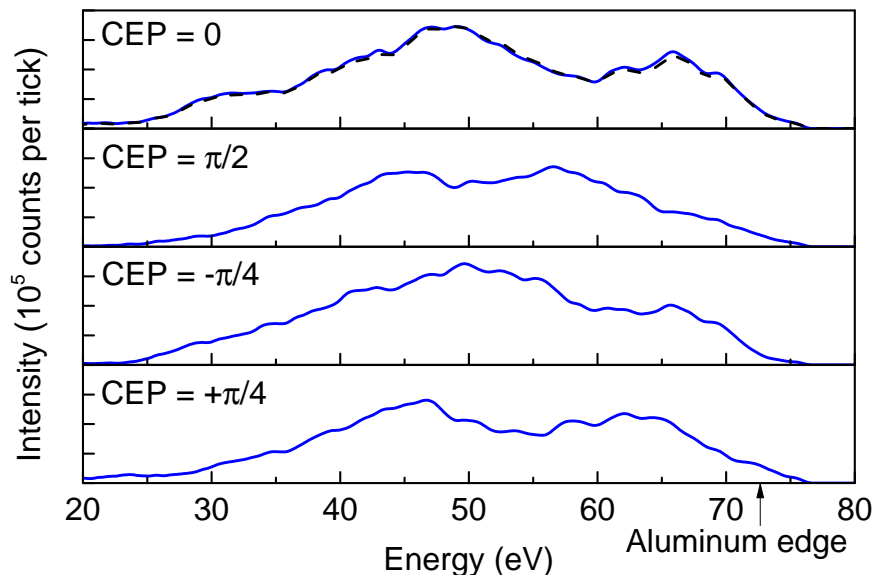


Figure 2.16: CEP dependence of HHG for few-cycle pulse with low dispersion. The difference in CE phase is adjusted with a precision of 0.15 rad and the identification with the absolute phase values is done according to the same principles as in Fig. 2.15. The black dashed line in the upper panel corresponds to a CE phase of π and reproduces the spectrum for CE phase of 0. The axes are scaled as in Fig. 2.13 with the filter transmission being accounted for.

When we changed the waveform to a sine, the center of the spectrum shifted to lower energies as expected. Furthermore, the total harmonic intensity decreases which can be attributed to aggravated phase matching conditions for the peak intensities of a sine waveform. However, this change is quite small and shows that the pulse duration has not yet reached that of a single cycle pulse. For such a short pulse, only the sine waveform can be expected to generate harmonics at a high efficiency. Despite of the high intensity of the central peak of the cosine waveform, all the electrons generated during this time are not accelerated to high energies anymore because the amplitude of the following peak is drastically reduced. On the other hand, the symmetry of the sine waveform allows for high ionization rates during the first peak as well as strong acceleration by the second peak.

This section has shown that the CEP is an important tool to adjust the conversion efficiency for the high order harmonics. Especially when it comes to isolating single attosecond pulses, it is essential to stabilize the CEP to a value at which the cutoff of the spectrum is unmodulated (cf. Sec. 2.1.1). Although generating high harmonics with a randomly fluctuating CE phase is still possible, the resulting spectrum will be a composite of spectra with different phase values which are superimposed due to the integration time of the spectrometer. Yet, in order to probe dynamics on or below the timescale of the attosecond pulse, it is crucial to generate the same pulse shape each time.

Chapter 3

Beam splitting via holey mirrors

Most experimental techniques used to study ultrafast phenomena are based on the same principle. A pump laser pulse with durations in the femtosecond or attosecond regime is used to trigger a process whose dynamic evolution is subsequently probed by a second laser pulse after an adjustable time delay. Typical signals recorded at each time step of the delay scan are the spectra of photoelectrons produced by an XUV pump pulse (e.g. attosecond streaking experiments), absorption of the probe pulse (e.g. transient absorption spectroscopy) or the momentum vectors of ionization fragments (e.g. COLTRIMS¹). In order to obtain a good signal to noise ratio, it is necessary to average the measured quantity over many laser shots. So it is important to synchronize the pump pulse precisely to the probe pulse because otherwise timing jitter will compromise the temporal resolution of the **pump-probe measurement**.

One way to achieve a high degree of synchronization is the use of a beamsplitter to build an actively stabilized Mach-Zehnder interferometer with a delay line in one arm. This is usually more feasible than the synchronization of two separate laser sources while still providing the ability to change the central wavelength of one of the pulses through nonlinear processes like HHG. The advantage of this method is that the frequency converted pulse is intrinsically synchronized to the input pulse.

However, conventional beamsplitters with high efficiency for pulses in the lower femtosecond regime are hardly available due to their broad frequency range. An alternative is the use of a holey mirror which transmits the central part of the beam and reflects the remaining part in the form of an annular beam. The functional principle of this beamsplitter is visualized in Fig. 3.1 on the next page.

This method imposes comparatively low losses on the beam since coatings for mirrors with high reflectances in the relevant spectral range are readily available. In addition, it is dispersion-free which means that it generates two spectrally and temporally identical

¹COLTRIMS stands for COLd Target Recoil Ion Momentum Spectroscopy.

pulses. Furthermore, the power ratio and the angle between the two beams can be chosen freely. The only disadvantage is that diffraction changes the spatial profile of the beams during propagation. The influence of this effect on the focusing properties of the beam are examined in this chapter using numerical methods along with experimental data.

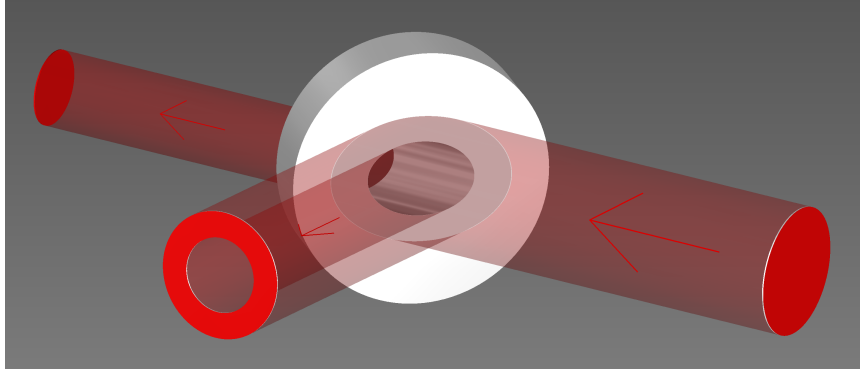


Figure 3.1: Principle of the holey mirror beamsplitter. A laser beam is split in an annular and a round beam.

3.1 Theory of diffraction for monochromatic light

Classical light fields like laser radiation are known to propagate as a wave. Diffraction is an immediate consequence of this concept and leads to effects like the divergence of laser beams, the limited size of focal spots and distortion of beam profiles upon clipping on an iris or other opaque objects in the beam path.

Although it is possible to directly solve the wave equation using finite element methods, it is advantageous to find approximations in order to reduce the computing time or to find analytical solutions. A significant step was performed by Kirchhoff and Fresnel by making the following assumptions on the diffraction imposed by a planar aperture [42]:

1. The distance from the aperture to the observation point is much longer than the wavelength.
2. The field and its derivative in direction of the aperture normal at a distance r from the aperture drop off at least as fast as $1/r$ as r approaches infinity.
3. The field in the transmissive section of the aperture plane is exactly the same as if the aperture was not there. That means that boundary conditions imposed by the rim of the aperture can be neglected.

These assumptions are clearly met by typical macroscopic apertures but become questionable as soon as the structure size approaches the wavelength, e.g. in nanostructured materials. Mathematical improvements subsequently lead to the well known **Rayleigh-Sommerfeld diffraction formula**[42]:

$$E(x, y, z) = \frac{z}{i\lambda} \iint_{\Sigma} dx' dy' \frac{e^{ikr}}{r^2} E(x', y', 0) \quad (3.1)$$

where $r = \sqrt{z^2 + (x - x')^2 + (y - y')^2}$ is the distance from the observation point (x, y, z) to the integration point (x', y') in the plane of the aperture Σ which is positioned at the longitudinal coordinate $z = 0$.

This formula can be simplified further by assuming that the point of observation is far away from the aperture compared to the transverse dimensions $|x - x'|$ and $|y - y'|$. In that case the value of the integral is dominated by the exponential function whose phase alternates on the scale of the wavelength. In consequence, one can neglect the minor changes of r in the denominator by setting it constant: $1/r^2 \approx 1/z^2$. For the highly oscillating exponential two approximations are commonly used which approximate r to the first or second order respectively:

$$r \approx \underbrace{z - \frac{xx' + yy'}{z}}_{\text{Fraunhofer approximation}} + \underbrace{\frac{x^2 + x'^2 + y^2 + y'^2}{2z}}_{\text{Fresnel approximation}} \quad (3.2)$$

The approximations are valid as long as the error introduced by them is much smaller than the wavelength. This imposes a lower limit on the distance z to the observation point which is given below for an aperture size of 1 cm at a wavelength of 780 nm. However, they remain accurate for a wider range as long as the aperture function varies slowly so that errors from neighboring oscillations cancel out.

Far-field limit (Fraunhofer approximation):

$$z \gg \frac{\pi}{\lambda} \max_{\Sigma} (x'^2 + y'^2) \approx 200 \text{ m}$$

Near-field limit (Fresnel approximation):

$$z \gg \sqrt{\frac{\pi}{4\lambda} \max_{\Sigma} ((x - x')^2 + (y - y')^2)} \approx 0.14 \text{ m}$$

So for most laser setups it is necessary to use the weaker Fresnel approximation to study diffraction effects. Another rewarding simplification can be made by using polar coordinates for radially symmetric apertures which reduces the integral from 2D to 1D:²

$$r_{Fresnel} = z + \frac{\rho^2 + \rho'^2 + 2\rho\rho'\cos(\theta - \theta')}{2z} \quad (3.3)$$

Performing the angular integration gives rise to the zeroth-order Bessel function J_0 and leaves the **Fresnel diffraction equation for radially symmetric apertures**.

$$E(\rho, z) = \frac{2\pi}{i\lambda z} \exp\left(ikz + \frac{ik\rho^2}{2z}\right) \int_0^\infty d\rho' \rho' \exp\left(\frac{ik\rho'^2}{2z}\right) J_0\left(\frac{k\rho\rho'}{z}\right) E(\rho', 0) \quad (3.4)$$

3.2 Theory of diffraction for polychromatic light pulses

In order to generate ultrashort laser pulses, a broad frequency spectrum is required. This is a consequence of the laws of the Fourier transform which give a lower bound for the time-bandwidth product of a given pulse shape. As an example, for pulses with a Gaussian temporal envelope it reads: $\Delta\nu \cdot \Delta\tau \geq 0.441$.³ Currently ultrabroadband oscillators spanning more than one octave can be realized technically [43, 44]. Since diffraction intrinsically depends on the wavelength, it is necessary to take the whole spectrum into account when examining the propagation and focusing of ultrashort laser pulses. In order to gauge the severity of this effect it is studied on pulses whose electric field is initially Gaussian in the temporal and radial domain as given below⁴. The calculations presented in this subsection are based on Ref. [45, 46].

$$E(x, y, z = 0, t) = E_0 \exp\left(-\frac{x^2 + y^2}{w_0^2} - \frac{t^2}{T^2} + i\omega_0 t\right) \quad (3.5)$$

The evolution of the field is determined by the wave equation:

$$\frac{\partial^2 E}{\partial x^2} + \frac{\partial^2 E}{\partial y^2} + \frac{\partial^2 E}{\partial z^2} = \frac{1}{c^2} \frac{\partial^2 E}{\partial t^2} \quad (3.6)$$

Solving the equation can be simplified by rewriting the field using its Fourier transform \tilde{E} :

$$E(x, y, z, t) = \frac{1}{(2\pi)^{3/2}} \iiint_{\mathbb{R}^3} dk_x dk_y d\omega \tilde{E}(k_x, k_y, z, \omega) e^{i(k_x x + k_y y + \omega t)} \quad (3.7)$$

² (ρ, θ) and (ρ', θ') are the polar coordinates for the point (x, y) and (x', y') respectively.

³ $\Delta\nu$ ($\Delta\tau$) is the FWHM of the temporal (spectral) intensity function.

⁴ ω_0 is the carrier frequency and w_0 (T) is the $1/e$ field width in the radial (temporal) dimension.

Inserting Eq. 3.7 in Eq. 3.6 and requiring paraxial propagation ($k_x^2 + k_y^2 \ll k_z^2$) yields:

$$\begin{aligned}\tilde{E}(k_x, k_y, z, \omega) &= \tilde{E}_0(k_x, k_y, z=0, \omega) \exp\left(-iz\sqrt{\frac{\omega^2}{c^2} - k_x^2 - k_y^2}\right) \\ &\approx \tilde{E}_0(k_x, k_y, z=0, \omega) \exp\left(-i\frac{\omega}{c}z + i\frac{k_x^2 + k_y^2}{2\omega/c}z\right)\end{aligned}\quad (3.8)$$

The paraxial approximation can be shown to be equivalent to the Fresnel approximation (Eq. 3.2) because both assume parabolic wave fronts [47]. In the above equation \tilde{E}_0 is the Fourier transform of the initial field given by Eq. 3.5:

$$\tilde{E}_0(k_x, k_y, \omega) = E_0 \frac{w_0^2 T}{2^{3/2}} \exp\left(-\frac{k_x^2 + k_y^2}{4} w_0^2 - \frac{(\omega - \omega_0)^2}{4} T^2\right)\quad (3.9)$$

Now one can perform the inverse Fourier transform on the spatial dimensions using Eq. 3.7:

$$\hat{E}(x, y, z, \omega) = \frac{E_0 T}{2^{1/2}} \beta(z, \omega) \exp\left(-i\frac{\omega}{c}z - \beta(z, \omega) \frac{x^2 + y^2}{w_0^2} - \frac{T^2}{4} (\omega - \omega_0)^2\right)\quad (3.10)$$

where $\beta(z, \omega) = \frac{q(0)}{q(z)} = \frac{1}{1 - i2zc/(\omega w_0^2)}$ and $q(z) = z + iz_R$ is the Gaussian beam parameter.⁵

The **spatio-temporal diffraction formula for Gaussian pulses** can be obtained by numerically performing the inverse Fourier transform on Eq. 3.10:

$$E(x, y, z, t) = \frac{1}{(2\pi)^{1/2}} \int_{\mathbf{R}} d\omega \hat{E}(x, y, z, \omega) e^{i\omega t}\quad (3.11)$$

In the continuous wave limit ($T \rightarrow \infty$) one recovers the well known results for a single frequency Gaussian beam as expected. In this situation, the beam propagation is determined by the Rayleigh length z_R after which the beam has doubled its cross section. It depends linearly on the frequency and takes on a value of around 100 m for a typical laser setup.⁶ However, propagation distances are usually much smaller which means that the different frequencies comprising the pulse all diverge to a similar extent. As a consequence, the frequency composition and the pulse duration are essentially the same at different positions in the beam. This is evident from Eq. 3.10 as well, because $\beta \rightarrow 1$ for $z \ll z_R$ leaving the spectrum of the initial Gaussian pulse displaced by the propagation time z/c .

⁵ $z_R = \frac{\omega w_0^2}{2c}$ is the Rayleigh length.

⁶The laser is assumed to have a central wavelength of $\lambda_0 = 780$ nm and 1/e field width of $w_0 = 5$ mm.

Apart from this near field solution, another analytical solution for Eq. 3.11 can be derived for the far field, i.e. $z \gg z_R$ which is discussed in Ref. [48]. For intermediate distances though, it is necessary to rely on numerical methods.

Unlike during free propagation, diffraction plays a non-negligible role when it comes to focusing ultrashort pulses. To this end, the calculation is adapted to include a focusing element with focal length f placed at the initial beam waist. In the ideal case, i.e. using a parabolic mirror, its effect can be represented as a retardation in time depending on the radial position in the beam: $t \rightarrow t + \rho^2 / (2fc)$. This shift in time corresponds to an additional phase $\exp(i\omega\rho^2 / (2fc))$ in frequency space. It can be added by substituting $1/w_0^2 \rightarrow 1/w_0^2 - i\omega / (2fc)$ in Eq. 3.5 yielding:

$$\hat{E}(\rho, z, \omega) = \frac{E_0 T}{2^{1/2}} \gamma(z, \omega) \exp\left(-i\frac{\omega}{c}z + \gamma(z, \omega) \left(i\frac{\omega}{c} \frac{\rho^2}{2f} - \frac{\rho^2}{w_0^2}\right) - \frac{T^2}{4}(\omega - \omega_0)^2\right) \quad (3.12)$$

where $\gamma(z, \omega) = \frac{1}{1 - i2zc/(\omega w_0^2) - z/f}$ describes the coupling between the temporal and spatial domain.

As a final result, the **spatio-temporal diffraction formula for focused Gaussian pulses** can be obtained by applying the inverse Fourier transform on Eq. 3.12.

3.3 Diffraction induced by holey mirrors

A main concern that may come to mind before utilizing holey mirrors is that the diffraction introduced by the hole might lead to distortions of a subsequent focus along with a reduced peak intensity. In order to address this issue, we implemented a numerical simulation of the diffraction effects using the formulas derived in the previous section.

3.3.1 Influence on the propagation

At first, we studied the effects of diffraction on a monochromatic Gaussian beam split by a holey mirror and its subsequent focusing properties. To this end, the radial diffraction integral (Eq. 3.4) was integrated numerically using Mathematica's NIntegrate algorithm and the results are compared to a measurement made with a continuous wave helium-neon laser ($\lambda = 632.8$ nm).

To check the validity of the numerical implementation, we first performed the calculations without the beamsplitter, i.e. calculating the propagation and focusing for a Gaussian beam. The results agree perfectly with the analytical predictions for the divergence, the focal waist size and the radius of curvature of the beam [49].

The mode of the laser used for the experiment can be well described by the Gaussian TEM00-mode. It was expanded to a waist size of $w_0 = 2.7$ mm and the holey mirror (hole radius = 0.5 mm) was placed at the waist position. Subsequently, we recorded two dimensional beam profiles for the reflected part of the beam using a CCD camera with suitable neutral density (ND) filters. From this data, the radial profiles were extracted by integrating over an angle of 30° . In order to compare them with the simulation they are scaled such that the radially integrated intensity coincides with the value from the simulation. This accounts for fluctuations in the laser intensity, different exposure times and ND filters. The results are shown in Fig. 3.2.

At first, we examined the propagation of the hollow beam up to a distance of 6 m. Unlike expected from geometrical optics, a small high intensity peak emerges in the center of the hole right after the mirror. This pattern is known as Poisson spot and arises due to the fact that all spherical waves emerging from a small ring around the hole of the mirror travel the same distance to a given point on the optical axis and thus interfere constructively [49].

During propagation the modulation frequency in the beam profile decreases. This can be understood intuitively since interference changes from constructive to destructive if the distance of the observer to the aperture $r = (z^2 + \rho^2)^{1/2}$ changes by half the wavelength. At a plane close to the aperture this difference can already be achieved by a small displacement $\delta\rho$ in radial direction whereas the same displacement at a plane far away from the aperture barely changes the distance r . This translates into a modulation frequency which depends on the propagation distance z .

Interestingly, the Gaussian beam profile is nearly restored after a propagation distance of 30 m, which is about the Rayleigh length of the initial beam ($z_R = 35$ m). This self-healing property is known to be inherent to a variety of diffractive and non-diffractive beams [50].

As a second step, we placed a lens with the focal length $f = 20$ cm in the beam path 60 cm behind the holey mirror to study the focusing properties of the propagated beam. Due to the smaller waist size, the beam divergence is drastically increased which means that similar characteristics than in case of free propagation arise already at shorter distances. A special feature can be seen 10 cm behind the focus where the imaging equation $1/b + 1/g = 1/f$ is fulfilled.⁷ Here, we observed a downscaled version of the initial beam profile albeit some fast oscillations around the rim of the hole. These can be attributed to a clipping effect since both, the optics and the numerical calculation only account for a finite beam width. Since the imaging equation can be derived in the framework of the Fresnel approximation, the experimental observation of this feature is a good proof of the theory.

⁷ $g = 60$ cm is the object distance, $f = 20$ cm is the focusing length and $g = 30$ cm is the image distance.

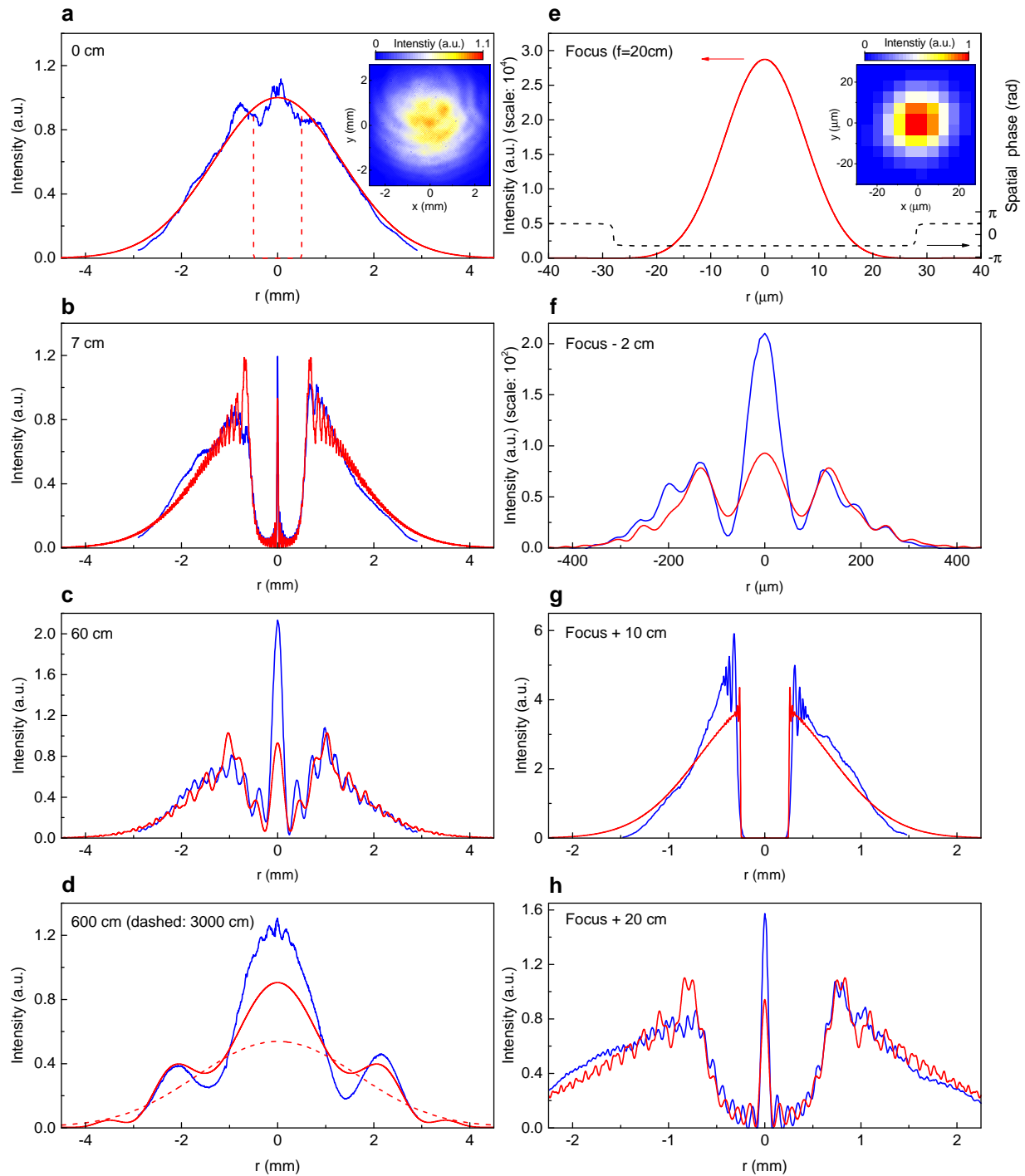


Figure 3.2: Radial intensity profiles of a beam reflected off a holey mirror and subsequently focused by a lens (blue: measurement, red: simulation). Caption is continued on next page.

Figure 3.2: (Previous page.) Initial profile in front of mirror (**a**) is fitted with a Gaussian and used as input for the simulation (red dashed in a: hole introduced by mirror, inset in a: 2D heatmap of measured initial distribution). All intensity scalings correspond to an initial maximum intensity of 1. Diffraction leads to formation of Poisson spot which is shown for propagation distances of 7 cm (**b**) and 60 cm (**c**). At 600 cm (**d**) the Gaussian shape of the profile starts to restore. Full restoration can be expected at 3000 cm (red dashed in d). The lens (focusing length 20 cm) is placed 60 cm behind the mirror. The simulation predicts that the focus (**e**) has a nearly Gaussian profile (black dashed: spatial phase indicating π phase jump, inset: 2D heatmap of measured focal spot). The patterns 2 cm before the focus (**f**) and 20 cm after the focus (**h**) show similar characteristics to the free propagation case. 10 cm after the focus (**g**) a scaled copy of the initial intensity distribution can be observed.

The most interesting region for experiments is the focus itself. Here, the simulation predicts a nearly Gaussian beam profile. The only difference is that a phase jump of π occurs at a radius with negligible intensity. Using different parameters for the setup shows that the field has a zero crossing at this radial position. However, this kink generally occurs in the low intensity part of the beam and is only a small deviation from an otherwise Gaussian profile. This phenomenon is known from circular airy beams where such a phase jump appears at every radial zero crossing of the field [51]. Unfortunately the focal intensity distribution cannot be measured at high resolution due to the limited pixel size of the CCD camera. However, the overall extent of the focus is in line with the simulation.

Overall, the calculation agrees well with the experimental results proving its validity. Especially the frequency of the modulations in the radial profile is reproduced correctly as well as the divergence of the beam. However, the amplitude of the central peak is predicted to be lower. This might have several reasons. First of all, the employed ND filter has a structure which also causes diffraction that results in parallel stripes in the beam profile. As an example, the beam profile is shown as an inset in Fig. 3.2. These modulations mostly average out due to the radial integration but affect the peak height to some extent. Furthermore, the diffraction patterns depend crucially on the shape and position of the hole relative to the beam. Tiny deviations from its circularity or back reflections from the walls of the hole due to non-ideal alignment are likely to have caused the discrepancies.

3.3.2 Influence on the focusing properties

For experiments with high power laser radiation it is not feasible to measure the focal intensity directly because no material can resist such high intensities. Instead it is possible to use a gas target placed in the focus as a probe. From a spatially resolved measurement of the ionization yield for different levels of ionization one can then infer the intensity distribution [52]. However, this method involves great experimental effort. A quick and widely used alternative is to assume a Gaussian beam profile for the initial beam. In

that case the focus also has a Gaussian profile whose waist size w_{Foc} can be calculated analytically [49]:

$$w_{Foc} = w_0 \frac{f}{\sqrt{(f-z)^2 + z_R^2}} \approx \frac{f\lambda}{\pi w_0} \quad (3.13)$$

where z is the distance from the initial beam waist with size w_0 to the focusing element with focusing length f and z_R is the Rayleigh length of the initial beam. The approximation holds for beams with large diameters ($z_R \gg |z - f|$) which is usually satisfied for high intensity beams. In the following we demonstrate that this formula keeps its validity for the part of a beam reflected off a holey mirror but needs to be modified for the transmitted part.

To begin with, we calculated the focal intensity distributions for the following experimental scenario: A monochromatic Gaussian beam with the waist size $w_0 = 5$ mm, wavelength $\lambda = 780$ nm and maximal intensity $I_0 = 1$ is split by an 80/20⁸ holey mirror beamsplitter, propagates freely for 1 m and is then focused by a parabolic mirror with focal length 60 cm. At first, the results for the reflected annular shaped beam are presented in Fig. 3.3.

Interestingly, the focus of the annular beam is nearly identical to that of a full Gaussian beam. This can be attributed to the self-healing properties of the beam observed in the propagation experiment (cf. Sec. 3.3.1). Deviations occur only in the outer, low intensity part of the focus and thus their influence can be neglected for most experiments.

To compare the results to a traditional beamsplitter⁹ we used Eq. 3.13 to calculate the properties of the corresponding Gaussian focus. Its radial extent $2w_0$ equals 60 μm , the longitudinal extent¹⁰ is 21 mm and the peak intensity for the reflected beam is $22.5 \cdot 10^3$ where an intensity of 1 corresponds to the maximal intensity of the collimated beam. In comparison, the focus generated after the holey mirror has the nearly same peak intensity $22.6 \cdot 10^3$ and an about 10 % reduced size (radial: 55 μm , longitudinal: 18 mm) owing to its broader low intensity wings.

All in all, the focus of the reflection has ideal properties for high-intensity experiments. As a general rule, large distortions of the focal volume can only be expected if the hole generated by the mirror is imaged close to the peak of the focus. According to the imaging equation $1/b + 1/g = 1/f$, this will only happen if the distance b between the beamsplitter and the focusing element is much larger than the focal length f . For the above example, this effect starts to become significant for propagation distances larger than 10 m. So in general, distortions of the focus can easily be avoided by designing a suitable laser setup.

⁸80/20 means 80 % reflectance and 20 % transmission.

⁹Traditional beamsplitter refers to an element that does not modify the beam profile but only splits the power between the reflected and the transmitted beam.

¹⁰The longitudinal focal size is defined as the full $1/e^2$ intensity width in longitudinal direction following the definition of the waist size.

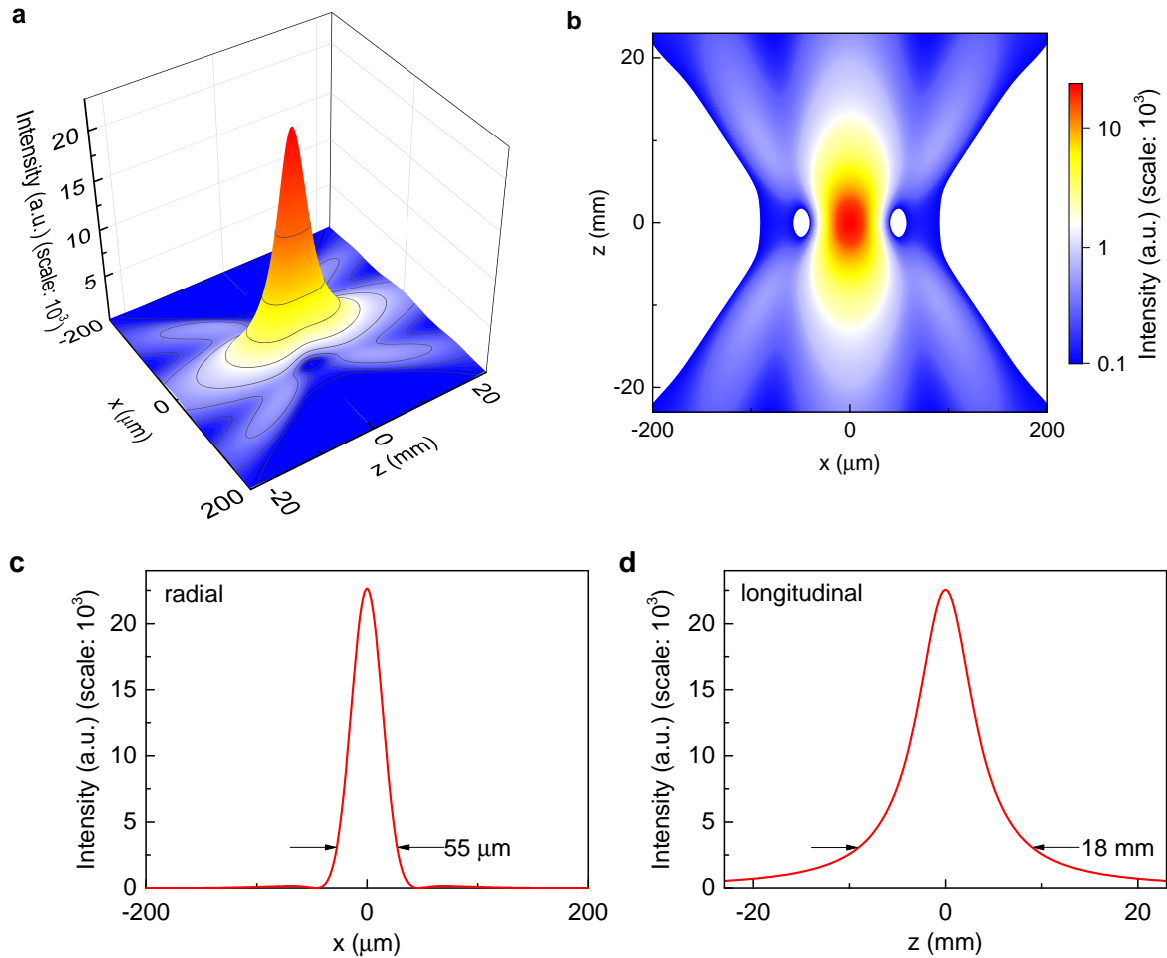


Figure 3.3: Calculated focal intensity distribution of a beam reflected off an 80/20 holey mirror beamsplitter and focused by a parabolic mirror with focusing length 60 cm. The distance between the mirrors is 1 m and the initial beam has a maximal intensity of 1. The linear 3D representation of the focus (a) shows a clear peak. Deviations from a Gaussian focus only occur at negligibly low intensities and are highlighted by the logarithmic color scaling. They are most prominent in the contour plot (b). The arrows in the radial (c) and longitudinal (d) profiles indicate the full $1/e^2$ intensity width of the focus.

However, large discrepancies arise for the focus of the transmitted beam visualized in Fig. 3.4. For the traditional beamsplitter the focus has a peak intensity of $5.6 \cdot 10^3$ and the same extent as for the reflected beam because the shape of the beam remains unchanged. However, using the same focusing length for the beam transmitted through the holey mirror yields a focus which is substantially broadened (radial: $233 \mu\text{m}$, longitudinal: 290 mm) and thus has a drastically reduced peak intensity of $0.3 \cdot 10^3$.

This effect is to be expected because the beam is cut off at a about a third of its initial width w_0 and smaller beams produce larger foci. Under the rough approximation that the transmitted beam has a Gaussian profile with the width $w_0/3$, Eq. 3.13 predicts a threefold increase in the radial extent, a ninefold increase in the longitudinal extent and a ninefold reduction of the peak intensity compared to focusing the beam transmitted by the traditional beamsplitter. Although this calculation underestimates the observed effects (radial: 4-fold increase, longitudinal: 16-fold increase, intensity: 19-fold decrease), it is useful to estimate their order of magnitude.

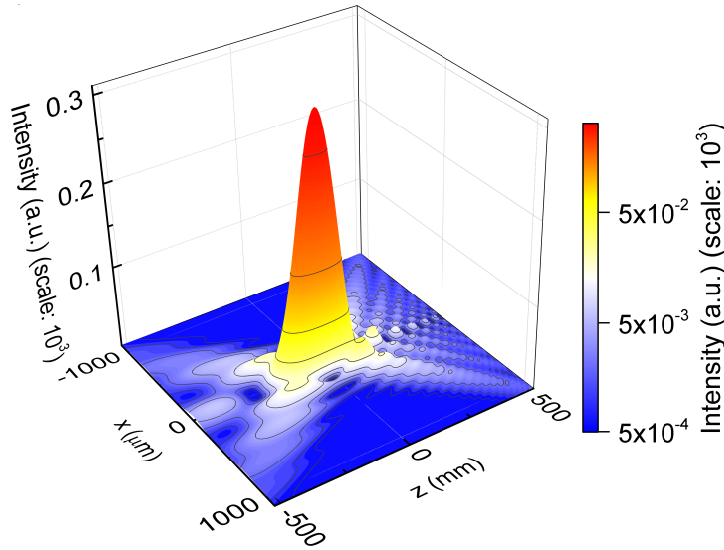


Figure 3.4: Calculated focal intensity distribution of a beam transmitted through an 80/20 holey mirror beamsplitter and focused by a parabolic mirror with focusing length 60 cm. The distance between the mirrors is 1 m and the initial beam has a maximal intensity of 1. The axes have a linear scaling whereas that of the colormap is logarithmic.

At the same time, Eq. 3.13 provides a solution for this problem since it predicts that the focal intensity scales inversely with the square of the focal length f . Assuming that this relation keeps its validity, one can achieve the same peak intensity like in case of the traditional beamsplitter by using the following formula to determine the focal length:

$$f_{corrected} = f \cdot \sqrt{\frac{I_{calculated}}{I_{expected}}} \quad (3.14)$$

where $f = 60$ cm is the focusing length used for the calculation, $I_{calculated} = 0.3 \cdot 10^3$ is the resulting peak intensity under these conditions and $I_{expected} = 5.6 \cdot 10^3$ is the peak intensity expected to be generated by the traditional beamsplitter (or any other peak intensity that one wants to obtain). The corrected focusing length for this example evaluates to 14 cm which generates the focal volume presented in Fig. 3.5 on the next page.

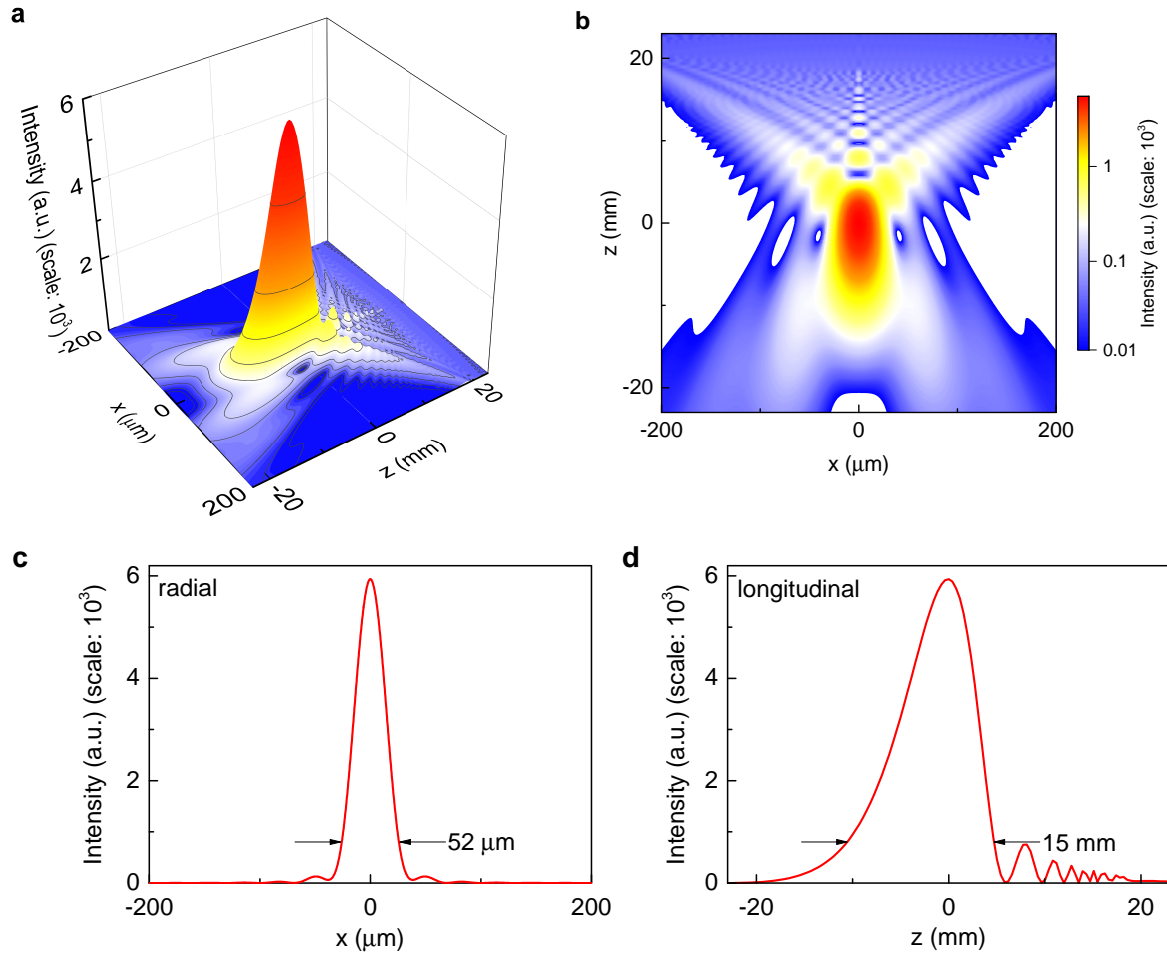


Figure 3.5: Calculated focal intensity distribution of a beam transmitted through an 80/20 holey mirror beamsplitter and focused by a parabolic mirror with focal length 14 cm. The distance between the mirrors is 1 m and the initial beam has a maximal intensity of 1. The linear 3D representation of the focus (a) shows a clear peak. Deviations from a Gaussian focus occur at lower intensities after the peak and are highlighted by the logarithmic color scaling. They are most prominent in the contour plot (b). The arrows in the radial (c) and longitudinal (d) profiles indicate the full $1/e^2$ intensity width of the focus.

Although the shape of this focus clearly deviates from that of a Gaussian, especially in the region behind the peak, its maximal intensity ($5.9 \cdot 10^3$) coincides with the one expected for the traditional beamsplitter up to a deviation of 5 %. Its radial extent ($52 \mu\text{m}$) is reduced by 13 % and its longitudinal extent (15 mm) by 29 % which indicates a stronger distortion of the focus compared to the case of the reflected beam. Although we believe that these deviations are noticeable in an experiment involving a nonlinear process, they are not as severe as to result in a drastic reduction of its outcome.

In order to generalize the findings for the holey mirror beamsplitter, we calculated the focal peak intensity in dependence of the hole size. Otherwise the scenario is kept the same, i.e. the beam propagates for 1 m before being focused over a length of 60 cm. Additionally, the shift in the focal position from the geometric focus at 60 cm is determined. This effect is well known for Gaussian beams and can be calculated analytically [49]:

$$\Delta f = z_{Foc} - f = \frac{f^2(z-f)}{(z-f)^2 + z_R^2} \approx \frac{f^2(z-f)\lambda^2}{\pi^2 w_0^4} \quad (3.15)$$

where z_{Foc} is the focal position and z is the distance from the waist of the initial beam to the focusing optic. The approximation holds for beams with large diameters ($z_R \gg |z-f|$). The results of the calculation are presented below in Fig. 3.6.

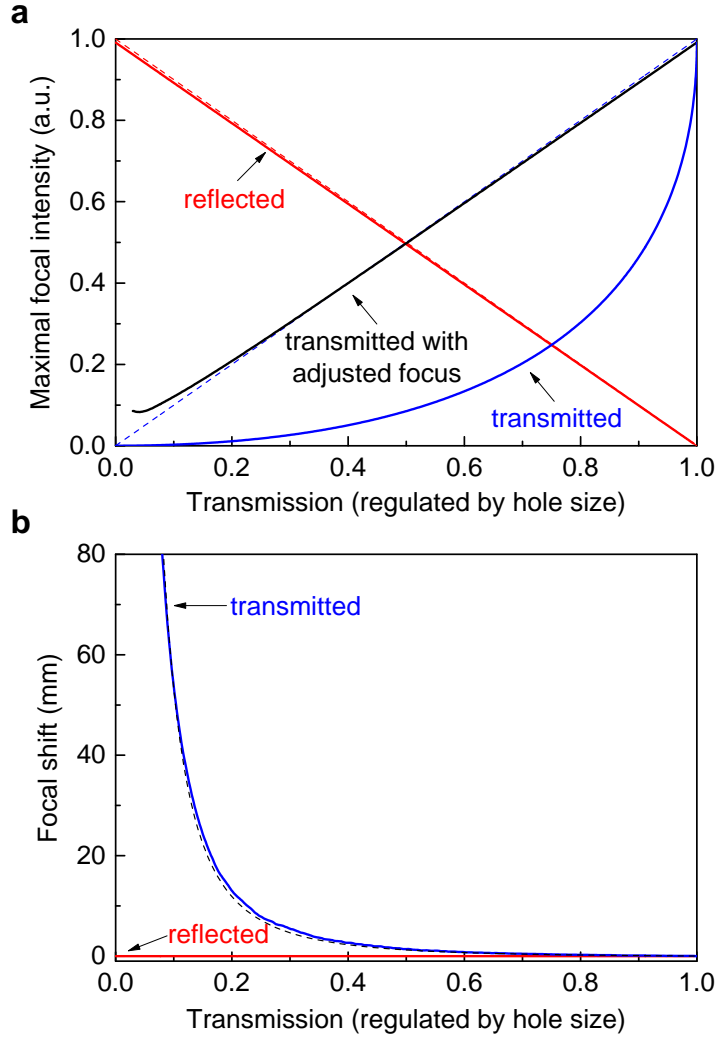


Figure 3.6: Dependence of the focal intensity (a) and the focal shift (b) on the hole size of a holey mirror beamsplitter. Caption is continued on next page.

Figure 3.6: (Previous page.) For a traditional beamsplitter the focal intensity of the transmitted (reflected) beam is proportional to the transmitted (reflected) power which is indicated by the dashed lines in a. The maximal intensity when focusing the reflection off a holey mirror shows almost the same dependence (red in a). However, the focus of the transmitted beam (blue in b) is heavily broadened and thus its peak intensity is drastically reduced. This effect can be compensated by correcting the focal length according to Eq. 3.14 (black in b). The beam transmitted through the holey mirror shows a strong focal shift (blue in b) that can be well described by the formula for a Gaussian beam (Eq. 3.15, black dashed in b) whereas the focus of the reflected beam shows no recognizable shift (red in b). For the calculation, a distance of 1 m between the beamsplitter and a parabolic mirror with focal length 60 cm were assumed and the intensities are normalized to the focal peak intensity obtained without the beamsplitter.

Interestingly, the focal shift for the beam reflected off the holey mirror is independent of the hole size of the mirror and on the order of that expected for the full beam ($\Delta f = 14 \mu\text{m}$). The transmitted beam on the other hand shows a strong focal shift on the order of several millimeters for a decreasing hole size. It can be well described by Eq. 3.15 when replacing the beam width w_0 with the hole size (h) reduced by a factor of about two. For this example the replacement $w_0 \rightarrow 0.56 h$ results in the best fit.

As it was shown in the previous section, the beam reflected off the holey mirror behaves very similar to a Gaussian beam in the vicinity of the focus. In particular, it reaches almost the same peak intensity than in the case of a traditional beamsplitter and should thus be used for nonlinear processes like HHG which depend strongly on the shape of the focus.

The maximal focal intensity of the transmitted beam on the other hand is strongly reduced when using the same focal length as for the reflected beam due to its smaller size. For a power transmission of below 40 % the focal intensity depends approximately quadratically on the hole size as expected from Eq. 3.13 for Gaussian beams. We could compensate this effect by using smaller focal lengths in the calculation which are adapted to the hole size according to Eq. 3.14. Doing so nearly yields the same peak intensity than for a traditional beamsplitter which shows that the scaling of the focal intensity with the inverse squared of the focal length is still valid for the transmitted beam at any given hole size.

Experimentally, one will always use a fixed hole size and focal length. In that case, small fluctuations in the size of the input beam cause variations in the focal position for low transmissions (here: $T \lesssim 50\%$) making a realignment necessary. One possibility to mitigate this effect is to design the laser system in a way that the waist of the input beam is positioned exactly one focal length before the focusing mirror which will prevent a focal shift according to Eq. 3.15. Another option is the use of a beam expander after the hole to restore the original size of the beam. Since the focal shift scales approximately inversely with the fourth power of the beam size, this will lower its influence substantially.

3.3.3 Effects due to spatio-temporal coupling

It is well known that using lenses to focus femtosecond laser pulses may significantly broaden and distort their temporal profile in the region of the focus due to spherical and chromatic aberration as well as the group velocity dispersion induced by the material [53, 54, 55]. This problem is usually addressed by using reflective optics with a suitable coating. However, with pulses approaching single cycle durations, their spectra become so broad that the intrinsic wavelength dependence of diffraction causes temporal broadening in the focus under otherwise ideal conditions.

To study this effect, we calculated the pulse duration in the focal volume numerically for beams with a Gaussian profile both in time and transverse dimension using the Fast-Fourier transform algorithm and Eq. 3.12. The scenario is kept similar to the previous one, i.e. a parabolic mirror with focal length 60 cm is used to focus pulses with a central wavelength of 780 nm and a radial extent w_0 of 5 mm. Since effects due to beam divergence can be neglected (cf. Sec. 3.2), the initial waist of the beam is placed on the focusing element.

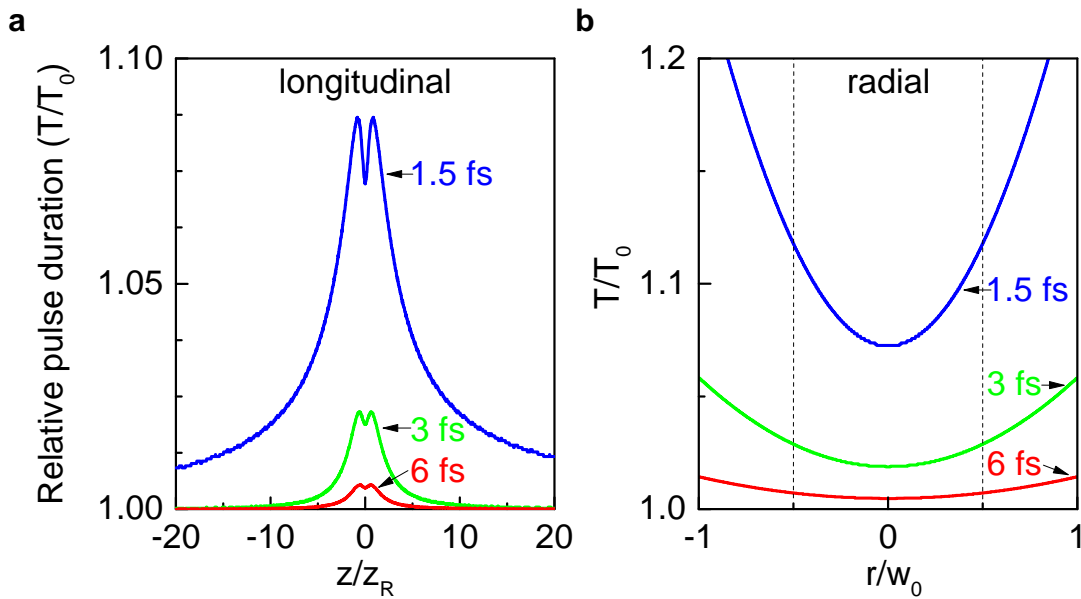


Figure 3.7: Calculated pulse duration in the focal volume (focusing length: 60 cm) along longitudinal (a) and radial (b) direction. The transverse profile of the pulse and its temporal envelope is assumed to be Gaussian at a central wavelength of 780 nm. The resulting pulse durations T are normalized to the initial $1/e$ field durations T_0 (cf. Eq. 3.5) which are indicated in the figure. The distances are normalized to the waist size $w_0 = 30 \mu\text{m}$ or the Rayleigh length $z_R = 3.6$ mm of the focal beam waist for the central wavelength. Due to the wavelength dependence of diffraction the pulse is temporally broadened in the focal volume. The effect has a stronger impact for shorter pulses especially when approaching sub-cycle pulses (in blue: $T_0 = 1.5$ fs). Dashed lines in (b) indicate the radius where the radial power density (i.e. $I(r) \cdot 2\pi r$) has its maximum for the central wavelength.

The results of the calculation (Fig. 3.7) reveal that a temporal broadening of up to several ten percent of the initial pulse duration can be expected for durations at or below that of a single cycle of the carrier ($T_{cycle} = 2.6$ fs). Intuitively the spatio-temporal coupling responsible for this phenomenon can be understood by looking at the focal properties of a Gaussian beam given by Eqs. 3.13 and 3.15. They state that the focus of a continuous wave beam with a smaller wavelength is located before that of one with larger wavelength and has a smaller size. Thus the different frequency components of the pulse are spread out over the focus resulting in a narrowing of the spectrum depending on the position in the beam. These distortions in frequency space translate into a broadening in the temporal domain.

Interestingly, the longitudinal profiles show a small dip at the position where the beam waist of the central wavelength is located. This can be attributed to the fact that the smaller wavelength components are already diverging at this position whereas the longer wavelength components are not yet completely focused. As a consequence, the distortion of the spectrum is partly compensated at this position.

In the radial direction, the temporal broadening increases strongly when moving away from the optical axis. This is to be expected because only in the center of the focus all pulses emerging from different positions in the initial beam profile will arrive at the same time. At any other position pulses that have propagated a longer distance will be superimposed with pulses that arrived earlier which broadens the total temporal profile.

The calculation also shows that the effects of spatio-temporal coupling depend strongly on the initial pulse duration and can be neglected for experiments with pulses encompassing more than a single cycle of the carrier. A similar trend can be expected for a beam split by a holey mirror and thus a generalization of the theory to arbitrary beam profiles is not investigated in this thesis.

3.4 Holey mirror beamsplitters in HHG

According to the calculations presented in the previous chapter, it is in general possible to generate high harmonics with both the beam reflected off and the beam transmitted through a holey mirror. All in all the reflected annular beam is supposed to be better suited because it generates a nearly undistorted Gaussian focal volume for any given hole size. This is advantageous because such a homogeneous distribution allows the intensity dependent phase matching condition for HHG to be met over a larger distance which increases the conversion efficiency (cf. Sec. 2.1.2). Additionally, the focus of the reflected beam is not shifted substantially if the size of the initial beam slightly changes upon modifications in the laser setup.

The position of the focus of the transmitted beam on the other hand reacts strongly to fluctuations in the initial beam size which necessitates frequent realignments of the gas target position. Although the peak intensity can be well adjusted by choosing a suitable focal length, the focus has a slightly smaller volume than that of a Gaussian due to distortions in its low intensity rim. This should affect the conversion efficiency negatively albeit the effect is probably too small to cause a strong reduction of the harmonic yield.

In the previous years many setups using annular beams for HHG have been demonstrated successfully [56, 57, 58]. In addition, the effect of different hole sizes on the harmonic yield has been studied experimentally in Ref. [59]. The referenced thesis reveals that the intensity of the harmonic radiation decreases with the hole size which is especially pronounced for harmonics in the cutoff region. However, the effect seems to be in line with the general intensity dependence of HHG and does not show strong detrimental effects emerging from the use of the annular beam. However, a comparison to the intensity dependence of the harmonics generated by the full beam was not provided.

The transmitted beam is usually not used for HHG. Due to the highly nonlinear intensity dependence of this process it is more efficient to generate high harmonics only once within the setup and split the resulting XUV beam afterwards if two time delayed XUV pulses are required. In this way several setups have been realized [60, 61, 62]. Nevertheless, the scaling of the harmonic intensity with the hole size is well known for the transmitted beam because this situation is equivalent to using an aperture in the beam for intensity regulation. Reducing the aperture size below the optimum results in a severe reduction of the harmonic yield. However, a quantitative comparison to a setup with an annular beam using the same laser source is not available.

In order to improve the predictions of the presented model for the holey mirror beam-splitter, it is crucial to use the two dimensional beam profile actually generated by the laser as an input for calculation because diffraction depends strongly on the initial shape. This can be achieved by implementing the full Fresnel diffraction equation (cf. Sec. 3.1) using the Fourier algorithm [63]. Doing so will allow to precisely determine the hole size and the focal lengths that need to be used to achieve a certain peak intensity.

Chapter 4

Conclusion

Both, the theoretical and the experimental part of this thesis demonstrate that high harmonic generation from gases is a fruitful tool for the production of attosecond pulses which can be adjusted by a wide range of parameters. However, the interplay between the influencing factors is quite complex such that the optimal settings are best determined experimentally.

In general, the wavelength of the driving laser λ_0 is the most important knob which adjusts the highest achievable energy of the harmonic radiation scaling proportional to $\lambda_0^{1.65 \pm 0.05}$. Yet, at the same time the conversion efficiency drops with $\lambda_0^{-5.5 \pm 0.5}$ for higher wavelengths which effectively limits the energies accessible by high harmonic generation to the soft X-ray region. A promising alternative is the generation of high harmonics from solids which potentially allows higher conversion efficiencies due to an increased particle density compared to gases [64].

Furthermore, it is shown that high levels of ionization of the target gas are the main factor limiting the yield in the cutoff region of the harmonic spectrum. This effect can be attributed to the formation of a defocusing "plasma lens" reducing the peak intensity of the driving field and worsened phase matching conditions due to an increased influence of electronic dispersion. Experimentally the pressure of the target gas was varied to control the density of the generated plasma. In good agreement with the theoretical expectations, an increased intensity of the cutoff harmonics could be observed for lower gas pressures.

In addition, it is demonstrated that the pulse duration and a precise control of the CE phase play a crucial role in achieving an unmodulated cutoff region needed for isolating single attosecond pulses. Only for a pulse consisting of very few cycles, the amount of plasma forming before its field peaks is still sufficiently low to enable efficient phase matching for the cutoff harmonics generated by its most intense half-cycle. Moreover, the CE phase of the pulse needs to be adjusted to ensure that the cutoff is produced exclusively by one half-cycle of the field such that the resulting attosecond burst can be filtered out spectrally.

It should be mentioned that free electron lasers are also capable of producing pulses with attosecond duration. Moreover, the energy of the generated pulses is orders of magnitude higher than in typical HHG setups and their spectra can extend up to the hard X-ray range [65]. However, due to the large size and cost of these facilities they only allow a limited number of experiments.

The second part of this thesis showed that holey mirrors are a well-functioning alternative to conventional beamsplitters for high power beams consisting of broadband pulses. Although the hole of the mirror introduces strong diffraction effects to both emerging beams while they propagate, they can still be focused to a largely undistorted focal volume. This means that their ability to generate high harmonics or cause other nonlinear processes is not impaired.

In particular, the calculation based on a Gaussian beam profile indicates that the reflected annular beam is focused to a focal volume which is nearly identical to that of the full beam regardless of the hole size. The transmitted beam on the other hand needs to be focused over a smaller focal length to compensate for its smaller size. In order to determine the correct focal length, it is demonstrated that the focal peak intensity still scales inversely with the focal length squared as it can be expected for a Gaussian beam. Unlike the reflected beam, the transmitted beam shows a strong focal shift on the order of several millimeters depending on the size of the hole. Conversely, if the size of the incident beam changes, the position of the focus will be shifted which necessitates a realignment of the target. Moreover, the focus of the transmitted beam is slightly narrower than that of a Gaussian which reduces the volume available to nonlinear optical processes. However, this effect is believed to be small compared to the power losses introduced by the coating of a conventional beamsplitter and its additional recompression stage. In conclusion, it can be stated that the reflected beam has more favorable properties for HHG.

In addition, the influence of diffraction on the focusing properties of ultrabroadband pulses were studied. Due to the intrinsic wavelength dependence of diffraction, the different frequencies comprising the pulse will be focused to slightly different positions and spot sizes. As a result, the spectrum of the pulse is distorted in the vicinity of the focus which leads to a temporal broadening. However, the effect on femtosecond pulses is only significant if their duration is below that of a single cycle of the carrier. As a consequence, most HHG experiments are not adversely affected by this spatio-temporal coupling.

Bibliography

- [1] S. Fujioka, Z. Zhang, N. Yamamoto, S. Ohira, Y. Fujii et al. *High-energy-density plasmas generation on GEKKO-LFEX laser facility for fast-ignition laser fusion studies and laboratory astrophysics*. Plasma Physics and Controlled Fusion **54** (2012), 124042.
- [2] A. McPherson, G. Gibson, H. Jara, U. Johann, T. S. Luk et al. *Studies of multiphoton production of vacuum-ultraviolet radiation in the rare gases*. J. Opt. Soc. Am. B **4** (1987), 595–601.
- [3] T. Brabec. *Strong Field Laser Physics*. Springer Science & Business Media, 1st ed. (2009).
- [4] M. Hentschel, R. Kienberger, C. Spielmann, G. Reider, N. Milosevic et al. *Attosecond metrology*. Nature **414** (2001), 509–513.
- [5] T. Gaumnitz, A. Jain, Y. Pertot, M. Huppert, I. Jordan et al. *Streaking of 43-attosecond soft-X-ray pulses generated by a passively CEP-stable mid-infrared driver*. Opt. Express **25** (2017), 27506–27518.
- [6] A. Sommer. *Ultrafast strong field dynamics in dielectrics* (2015).
- [7] L. Belshaw, F. Calegari, M. J. Duffy, A. Trabattoni, L. Poletto et al. *Ultrafast electron dynamics in an amino acid measured by attosecond pulses*. Conference on Lasers Electro-Optics Europe International Quantum Electronics Conference CLEO EUROPE/IQEC (2013).
- [8] M. Nisoli, P. Decleva, F. Calegari, A. Palacios, F. Martìn. *Attosecond electron dynamics in molecules*. Chem. Rev. **117** (2017), 10760–10825.
- [9] International Organization for Standardization. *Space environment (natural and artificial) - process for determining solar irradiances*. ISO 21348 (2007).
- [10] M. Ossiander, F. Siegrist, V. Shirvanyan, R. Pazourek, A. Sommer et al. *Attosecond correlation dynamics*. Nature Phys. **13** (2016).
- [11] R. W. Boyd. Academic Press, Burlington, 3rd ed. (2008).

- [12] W. Guoli, J. Cheng, A.-T. Le, C. D. Lin. *Influence of gas pressure on high-order-harmonic generation of Ar and Ne*. Phys. Rev. A **84** (2011).
- [13] M. Sayrac, A. A. Kolomenskii, S. Anumula, Y. Boran, N. A. Hart et al. *Pressure optimization of high harmonic generation in a differentially pumped Ar or H₂ gas jet*. Rev. Sci. Instr. **86** (2015), 043108.
- [14] E. Constant, D. Garzella, P. Breger, E. Mével, C. Dorrer et al. *Optimizing high harmonic generation in absorbing gases: Model and experiment*. Phys. Rev. Lett. **82** (1999), 1668–1671.
- [15] J. Rothhardt, M. Krebs, S. Hädrich, S. Demmler, J. Limpert et al. *Absorption-limited and phase-matched high harmonic generation in the tight focusing regime*. New J. Phys. **16** (2014), 033022.
- [16] A. Vernaleken, J. Weitenberg, T. Sartorius, P. Russbueldt, W. Schneider et al. *Single-pass high-harmonic generation at 20.8 MHz repetition rate*. Opt. Lett. **36** (2011), 3428–3430.
- [17] P. B. Corkum. *Plasma perspective on strong field multiphoton ionization*. Phys. Rev. Lett. **71** (1993), 1994–1997.
- [18] M. V. Ammosov, P. A. Golovinsky, I. Y. Kiyan, V. P. Kraĭnov, V. M. Ristic. *Tunneling ionization of atoms and atomic ions in an intense laser field with a nonhomogeneous space-time distribution*. J. Opt. Soc. Am. B **9** (1992), 1225–1230.
- [19] S. L. Chin, H. Xu. *Tunnel ionization, population trapping, filamentation and applications*. J. Phys. B **49** (2016), 222003.
- [20] R. Silva, P. Rivière, F. Morales, O. Smirnova, M. Ivanov et al. *Even harmonic generation in isotropic media of dissociating homonuclear molecules*. Sci. Rep. **6** (2016).
- [21] R. R. Alfano. *The Supercontinuum Laser Source*. 3rd ed. (2016).
- [22] M. Chini, K. Zhao, Z. Chang. *Broadband isolated attosecond pulses: Generation, characterization, and applications*. Nature Photonics **8** (2013).
- [23] M. Lewenstein, P. Balcou, M. Y. Ivanov, A. L’Huillier, P. B. Corkum. *Theory of high-harmonic generation by low-frequency laser fields*. Phys. Rev. A **49** (1994), 2117–2132.
- [24] M. Fieß. *Advancing attosecond metrology* (2010).
- [25] P. Colosimo, G. Doumy, C. I. Baga, J. Wheeler, C. Hauri et al. *Scaling strong-field interactions towards the classical limit*. Nature Phys. **4** (2008), 386–389.
- [26] C. Winterfeldt. *Generation and control of high-harmonic radiation* (2006).
- [27] B. K. Dinh. *Phase-matched high order harmonic generation and applications*.

- [28] F. Lindner, G. G. Paulus, H. Walther, A. Baltuška, E. Goulielmakis et al. *Gouy phase shift for few-cycle laser pulses*. Phys. Rev. Lett. **92** (2004), 113001.
- [29] M. Lewenstein, P. Salières, A. L’Huillier. *Phase of the atomic polarization in high-order harmonic generation*. Phys. Rev. A **52** (1995), 4747–4754.
- [30] A. Kramida, Yu. Ralchenko, J. Reader, NIST ASD Team. *NIST atomic spectra database (ver. 5.5.6)*. National Institute of Standards and Technology (2018).
- [31] B. L. Henke, E. M. Gullikson, J. C. Davis. *X-ray interactions: Photoabsorption, scattering, transmission, and reflection at $E = 50\text{--}30,000$ eV, $Z = 1\text{--}92$* . Atomic Data and Nuclear Data Tables **54** (1993), 181–342.
- [32] K. S. Budil, P. Salières, A. L’Huillier, T. Ditmire, M. D. Perry. *Influence of ellipticity on harmonic generation*. Phys. Rev. A **48** (1993), 3437–3440.
- [33] K. Z. Hatsagortsyan, M. Klaiber, C. Müller, M. C. Kohler, C. H. Keitel. *Laser-driven relativistic recollisions*. J. Opt. Soc. Am. B **25** (2008), 92–103.
- [34] H. Dachraoui, T. Auguste, A. Helmstedt, P. Bartz, M. Michelswirth et al. *Interplay between absorption, dispersion and refraction in high-order harmonic generation*. J. Phys. B **42** (2009), 175402.
- [35] C.-J. Lai, F. X. Kärtner. *The influence of plasma defocusing in high harmonic generation*. Opt. Express **19** (2011), 22377–22387.
- [36] T. Popmintchev, M.-C. Chen, A. Bahabad, M. Gerrity, P. Sidorenko et al. *Phase matching of high harmonic generation in the soft and hard X-ray regions of the spectrum*. Proceedings of the National Academy of Sciences **106** (2009), 10516–10521.
- [37] A. Paul, E. A. Gibson, X. Zhang, A. Lytle, T. Popmintchev et al. *Phase-matching techniques for coherent soft X-ray generation*. IEEE J. Quantum Electron. **42** (2006), 14–26.
- [38] A. Akil. *High intensity effects in bandgap materials* (2017).
- [39] J. Rauschenberger. *Phase-stabilized ultrashort laser systems for spectroscopy* (2007).
- [40] F. Lücking. *Carrier-envelope phase control for the advancement of attosecond pulse generation* (2014).
- [41] F. Krausz, M. Ivanov. *Attosecond physics*. Rev. Mod. Phys. **81** (2009), 163–234.
- [42] J. W. Goodman. *Introduction to Fourier Optics*. 3rd ed. (2005).
- [43] N. Leindecke, A. Marandi, R. L. Byer, K. L. Vodopyanov, J. Jiang et al. *Octave-spanning ultrafast OPO with 2.6–6.1 μm instantaneous bandwidth pumped by femtosecond Tm-fiber laser*. Opt. Express **20** (2012), 7046–7053.

- [44] Z. Wang, C.-Y. Wang, Y. Han, S. Cao, Z. Zhang et al. *Octave-spanning spectrum generation in Ti:sapphire oscillator*. Optics & Laser Technology **38** (2006), 641–644.
- [45] I. P. Christov. *Propagation of femtosecond light pulses*. Opt. Commun. **53** (1985), 364–366.
- [46] E. Karimi, C. Altucci, V. Tosa, R. Velotta, L. Marrucci. *Influence of generalized focusing of few-cycle gaussian pulses in attosecond pulse generation*. Opt. Express **21** (2013), 24991–24999.
- [47] R. Lee. *Electromagnetic waves in optoelectronics*. Lecture at National Tsing Hua University (2005).
- [48] R. W. Ziolkowski, J. B. Judkins. *Propagation characteristics of ultrawide-bandwidth pulsed gaussian beams*. J. Opt. Soc. Am. A **9** (1992), 2021–2030.
- [49] A. Dorsel, M. Klein, T. Hellmuth, T. Furtak. *Optik*. Springer Berlin Heidelberg (1988).
- [50] A. Aiello, G. S. Agarwal, M. Paúr, B. Stoklasa, Z. Hradil et al. *Unraveling beam self-healing*. Opt. Express **25** (2017), 19147–19157.
- [51] H. Deng, Y. Yuan, L. Yuan. *Annular arrayed-waveguide fiber for autofocusing airy-like beams*. Opt. Lett. **41** (2016), 824.
- [52] P. Tzallas, B. Bergues, D. Rompotis, N. Tsatrafyllis, S. Chatziathanassiou et al. *Time gated ion microscopy of light-atom interactions*. J. Opt. **20** (2018).
- [53] M. Kempe, U. Stamm, B. Wilhelmi, W. Rudolph. *Spatial and temporal transformation of femtosecond laser pulses by lenses and lens systems*. J. Opt. Soc. Am. B **9** (1992), 1158–1165.
- [54] M. Kempe, W. Rudolph. *Femtosecond pulses in the focal region of lenses*. Phys. Rev. A **48** (1993), 4721–4729.
- [55] G. O. Mattei, M. A. Gil. *Spherical aberration in spatial and temporal transforming lenses of femtosecond laser pulses*. Appl. Opt. **38** (1999), 1058–1064.
- [56] J. Peatross, J. L. Chaloupka, D. D. Meyerhofer. *High-order harmonic generation with an annular laser beam*. Opt. Lett. **19** (1994), 942–944.
- [57] F. Frank, C. Arrell, T. Witting, W. A. Okell, J. McKenna et al. *Invited review article: Technology for attosecond science*. Rev. Sci. Instr. **83** (2012), 071101.
- [58] P. M. Paul, E. S. Toma, P. Breger, G. Mullot, F. Augé et al. *Observation of a train of attosecond pulses from high harmonic generation*. Science **292** (2001), 1689–1692.
- [59] H. Wikmark. *A high-order harmonic pump-probe setup using annular-beam interferometers* (2016).

-
- [60] F. Campi, H. Coudert-Alteirac, M. Miranda, L. Rading, B. Manschwetus et al. *Design and test of a broadband split-and-delay unit for attosecond XUV-XUV pump-probe experiments*. Rev. Sci. Instr. **87** (2016), 023106.
- [61] P. Tzallas, D. Charalambidis, N. Papadogiannis, K. Witte, G. D Tsakiris. *Direct observation of attosecond light bunching*. Nature **426** (2003), 267–71.
- [62] E. J. Takahashi, P. Lan, O. D. Mücke, Y. Nabekawa, K. Midorikawa. *Attosecond nonlinear optics using gigawatt-scale isolated attosecond pulses*. Nature Commun. **4** (2013).
- [63] D. Mas, J. Garcia, C. Ferreira, L. M. Bernardo, F. Marinho. *Fast algorithms for free-space diffraction patterns calculation*. Opt. Commun. **164** (1999), 233 – 245.
- [64] Y. Sing You, Y. Yin, Y. Wu, A. Chew, X. Ren et al. *High-harmonic generation in amorphous solids*. Nature Commun. **8** (2017), 724.
- [65] S. Huang, Y. Ding, Y. Feng, E. Hemsing, Z. Huang et al. *Generating single-spike hard X-ray pulses with nonlinear bunch compression in free-electron lasers*. Phys. Rev. Lett. **119** (2017), 154801.

Acknowledgment

This thesis would not have been possible without the support of numerous people. I want to start by thanking my supervisor Dr. Martin Schultze for giving me the opportunity to work in his research group as a Bachelor's student. By sharing his extensive scientific knowledge with me during the past ten weeks, he gave me a comprehensive insight into ultrafast laser physics and provided valuable incentives for this thesis.

Furthermore, I am very thankful to all members of the ATTO group for their welcoming attitude and their patience in answering all my questions. Thank you, Julia Gessner, Keyhan Golyari, Marcus Ossiander, Malte Schröder and Florian Siegrist. In particular, I would like to thank Keyhan and Marcus who took their time to teach me all about the practical work in the laser lab. In addition, I owe Marcus a big thank you for proofreading this thesis.

Finally, I would like to mention my parents who have always supported me in so many ways. Thank you!

Erklärung zur Bachelorarbeit

Hiermit erkläre ich, die vorliegende Arbeit selbständig verfasst zu haben und keine anderen als die in der Arbeit angegebenen Quellen und Hilfsmittel benutzt zu haben.

Bachelor's thesis statement of originality

I hereby confirm that I have written the accompanying thesis by myself, without contributions from any sources other than those cited in the text and acknowledgments.

.....

Ort und Datum
Place and date

.....

Unterschrift
Signature